Soft Matter

Accepted Manuscript

This article can be cited before page numbers have been issued, to do this please use: C. J. Guido, J. P. Binagia and E. S. G. Shaqfeh, *Soft Matter*, 2019, DOI: 10.1039/C8SM02518E.

ROYAL SOCIETY OF CHEMISTRY

rsc.li/soft-matter-journal

View Article Online
DOI: 10.1039/C8SM02518E

Soft Matter

ARTICLE TYPE

Cite this: DOI: 10.1039/xxxxxxxxxx

Three-Dimensional Simulations of Undulatory and Amoeboid Swimmers in Viscoelastic Fluids†

Jeremy P. Binagia,‡[a] Christopher J. Guido,‡[a] and Eric S.G. Shaqfeh[a,b,c]

Received Date
Accepted Date

DOI: 10.1039/xxxxxxxxxx

www.rsc.org/journalname

Microorganisms often move through viscoelastic environments, as biological fluids frequently have a rich microstructure owing to the presence of large polymeric molecules. Research on the effect of fluid elasticity on the swimming kinematics of these organisms has usually been focused on those that move via cilia or flagellum. Experimentally, Shen (Shen *et al., Physical Review Letters*, 2011, **106**, 1–4.) reported that the nematode *C. elegans*, a model organism used to study undulatory motion, swims more slowly as the Deborah number describing the fluid's elasticity is increased. This phenomenon has not been thoroughly studied via a fully resolved three-dimensional simulation; moreover, the effect of fluid elasticity on the swimming speed of organisms moving via euglenoid movement, such as *E. gracilis*, is completely unknown. In this study, we discuss the simulation of the arbitrary motion of an undulating or pulsating swimmer that occupies finite volume in three dimensions, with the ability to specify any differential viscoelastic rheological model for the surrounding fluid. To accomplish this task, we use a modified version of the Immersed Finite Element Method presented in a previous paper by Guido and Saadat in 2018 (Saadat *et al., Physical Review E*, 2018, **98**, 063316.). In particular, this version allows for the simulation of deformable swimmers such that they evolve through an arbitrary set of specified shapes via a conformation-driven force. From our analysis, we observe several key trends not found in previous two-dimensional simulations or theoretical analyses for *C. elegans*, as well as novel results for the amoeboid motion. In particular, we find that regions of high polymer stress concentrated at the head and tail of the swimming *C. elegans* are created by strong extensional flow fields and are associated with a decrease in swimming speed for a given swimming stroke. In contrast, in two dimensions these regions of stress are commonly found distributed along the entire body, likely owing to the lack of a third dimension for polymer relaxation. A comparison of swim speeds shows that the calculations in two-dimensional simulations result in an over-prediction of the speed reduction. We believe that our simulation tool accurately captures the swimming motion of the two aforementioned model swimmers and furthermore, allows for the simulation of multiple deformable swimmers, as well as more complex swimming geometries. This methodology opens many new possibilities for future studies of swimmers in viscoelastic fluids.

1 Introduction

The study of the motion of microorganisms has many applications, ranging from human fertility[1] to disease prevention[2,3]. A clear understanding of locomotion at these small length scales can also aid in the design of synthetic swimmers, which are utilized in a variety of biomedical applications, including targeted drug delivery[4–15]. Because these organisms are typically of micron size, the Reynolds number associated with their motion is vanishingly small[16]. This has allowed researchers to use the tools of low Reynolds number hydrodynamics (e.g. linearity, superposition, time reversibility) to develop many interesting insights into microorganism locomotion[17,18]. However, while the study of locomotion at low Reynolds number in Newtonian fluids is well-developed, relatively little is known about locomotion in complex fluids, e.g. fluids that exhibit some degree of memory or shear-dependent viscosity. This is significant in that the vast majority of biological fluids are actually non-Newtonian, usually since they

[a] Department of Chemical Engineering, Stanford University, Stanford, CA 94305, USA
[b] Department of Mechanical Engineering, Stanford University, Stanford, CA 94305, USA
[c] Institute for Computational and Mathematical Engineering, Stanford University, Stanford, CA 94305, USA

† Electronic Supplementary Information (ESI) available: Supplementary videos of *C. elegans* and the amoeboid are included. See DOI: 10.1039/cXsm00000x/

‡These authors contributed equally to this work.

View Article Online
DOI: 10.1039/C8SM02518E

possess a rich microstructure because they are laden with large biomolecules. The lack of progress in understanding undulatory locomotion in these fluids can be directly attributed to the difficult non-linearities complex fluid constitutive models present. These non-linearities prevent the use of many of the tools that have facilitated the analysis of swimming motion in Newtonian fluids. Moreover the behavior of complex fluids in the presence of an active forcing is oftentimes markedly different from that exhibited by Newtonian fluids. For example, it was shown recently that fluid elasticity promotes the alignment and collective swimming behavior of sperm cells, suggesting that fluid elasticity could actually play a central role in successful fertilization[19].

To gain an understanding of how microorganisms move utilizing cilia of flagellum at low Reynolds number, researchers have analyzed the motion of the much larger nematode *C. elegans* in a very viscous fluid as a convenient scale-up experiment of microscopic undulatory motion[20]. *C. elegans* swimming experiments have been conducted both in Newtonian fluids[21,22], as well as in more complex fluids that exhibit a significant degree of fluid elasticity and shear-dependent rheology[23–25]. In general, it has been found that *C. elegans* swims more slowly as the elasticity of the fluid is increased[23].

Undulatory swimming models have been studied both numerically and theoretically. For example, Lauga found that Taylor's swimming sheet[26] in the limit of small wave amplitude swims more slowly as the effect of fluid elasticity becomes more pronounced (i.e. increasing Deborah number)[27], in rough agreement with the aforementioned experimental results. Later, Riley and Lauga considered the waving sheet model in a more general framework, showing that fluid elasticity does not always lead to a decrease in swimming speed[28,29]. Similar perturbation analyses have been completed for the motion of waving filaments, and these researchers also found that fluid elasticity tends to hinder locomotion[30,31]. Several prior computational studies have also been conducted to understand the variation of swimming speed with Deborah number beyond the applicability of perturbation theory. Teran *et al.* found in their 2D simulations of a finite-length line-element model that fluid elasticity actually leads to an increase in the swimming speed[32]. There, they showed that regions of large polymer stress accumulate near the swimming body and are associated with the change in swimming speed. In this study we will show that such regions of large stress arise from extensional flow points near the head and tail of the swimmer. It was later shown by Thomases *et al.* that either an increase or decrease in swimming speed can be observed depending on the type of swimming motion, i.e, if it is driven by large head or tail undulations (called a burrower and kicker respectively) and on the degree to which the prescribed target curvature in these models is actually achieved (i.e, whether it is a "soft" or "stiff" swimmer)[33,34]. More recent work by Salazar *et al.* found that a speed increase could only be observed if the polymer stress diffusion coefficient used in these studies was sufficiently large[35].

A series of studies related to swimming motion in 3D have been conducted recently for both small amplitude swimming in shear thinning fluids and for a different organism, *C. reinhardtii*, which swims with a breaststroke-like gait via two anterior flagella[14,36]. The study of 3D locomotion in shear thinning fluids demonstrated that the calculation of quantities that depend upon flow derivatives (e.g. shear rate) can be *qualitatively* different when computed in 2D vs. 3D[36]. For example, the author found for a small-amplitude undulatory swimmer modeled as a cylinder that the maximum shear-rate was located at the surface of the swimmer (as one might expect). However, the same calculation repeated for a waving sheet predicted that the maximum occurs some distance away from the swimmer (with *decreasing* shear rate as one moves closer to the surface). While these calculations were illustrated using shear thinning rheology, this work suggested that similar errors are likely to occur in viscoelastic fluids as well. While the above study of Montenegro-Johnson was done in the context of the undulatory motion of *C. elegans*, recently the flagellar motion of *C. reinhardtii* was succesfully simulated by Li *et al.* through the use of a 3D immersed boundary method. This group of researchers made a number of interesting observations, including that in 3D, polymer stresses accumulate near the tips of the flagellar structures, but these structures were only resolved as line elements (i.e. a series of connected points)[14]. More recently, members of the same group considered the steady motion of slender objects in viscoelastic fluids to understand more generically how the orientation of these elongated structures is related to regions of polymer stress in the surrounding flow[37]. The purpose of our work seeks to build on these results and examine large amplitude undulatory swimming of *C. elegans* in a viscoelastic fluid, with the body of the nematode being fully meshed in 3D. Additionally, we seek to analyze the flow field surrounding the undulatory swimmer to further understand its relationship to the organism's calculated swimming speed.

In summary, the effect of fluid elasticity on swimming motion is a complex topic and is clearly not fully understood. While the previously mentioned studies in 2D have provided valuable insights into swimming behavior in viscoelastic fluids, none of these studies have considered fully three-dimensional flow driven by a fully-resolved immersed body (i.e. finite thickness rather than a series of points). These features are likely critical for accurate prediction of swimming kinematics as suggested by previous results for small amplitude undulatory motion in a shear thinning fluid[36]. Furthermore, these 2D studies utilize relatively high viscoelastic viscosity ratios ($\beta = \eta/\eta_0$) while the experiments by Shen *et al.* were conducted at relatively low values of β[23]. In our work, we seek to explore the effect of the viscosity ratio on the results as well as to investigate the full three-dimensional behavior of the flow to demonstrate that these must be taken into account to gather a complete understanding of this problem.

While considerable work has been done concerning swimmers that swim via undulatory or helical motion[38–40], there exist relatively few studies on organisms at low Reynolds number that move via more exotic body deformation methods, such as the euglenoid movement (i.e. metaboly) exhibited by *Euglena*. In particular, it was recently found that *Dictyostelium* amoebae and human neutrophils could freely swim in solution at speeds comparable to those at which they crawl across substrates by undergoing extensive deformations in shape[41,42]. Aiming to model this phenomena, Farutin and Misbah simulated a vesicle with a simple

View Article Online
DOI: 10.1039/C8SM02518E

force distribution to illustrate how such an organism could propel itself through deformations of its membrane[43]. In later work, the effect of confinement on the swimming kinematics of these types of swimmers was quantified in 2D[44,45]. More recently, this model has been extended to 3D flows in Newtonian fluids, and the effect of cytoskeleton elasticity has been considered by allowing for changes in membrane area by modeling the swimmer as a capsule rather than a vesicle[46]. However, to our knowledge there have been no such studies examining this swimming behavior in a viscoelastic fluid. We demonstrate in this work that the reduction in swimming speed for amoeboid motion is quite similar to that found for *C. elegans*, and that the physics of speed reduction show several similarities despite how different the two modes of swimming are .

In this manuscript, we compare fully three-dimensional computational results for two different model organisms: the undulatory motion of *C. elegans* and the amoeboid motion. In regards to the undulatory motion, we find that 2D simulations over-predict the reduction in swimming speed compared to 3D simulations. From an analysis of the surrounding flow field, we note that this is likely associated with the high concentration of polymer stress near the head and tail of the swimmer (in 2D, this stress is found along the entire body for[32,33,35]). Furthermore, we use a local decomposition of the flow field to show explicitly that these regions of high polymer stress are created by strong extensional flow at said locations. For the amoeboid motion, we see a trend in swim speed directly analogous to that of *C. elegans*: a monotonic decrease in speed increasing with Deborah number ultimately approaching a value that appears to be asymptotic for large De. For the amoeboid, we also calculate the swimming power expenditure and efficiency as a function of De. We find that the amoeba spends a disproportionate amount of energy even with the reduction of speed it incurs, thus leading to a decrease in swimming efficiency with De.

2 Methodology

2.1 Governing Equations for Swimming Bodies

We consider the dynamic problem of an incompressible elastic body suspended in an incompressible Newtonian or complex polymeric fluid media, where the suspended body is a neutrally buoyant, active swimmer. The total domain under consideration is defined to be Ω which will be broken into two sub-domains Ω^{f} and Ω^{s} which represent the volume of the fluid and the swimmer respectively. The governing equations are conservation of momentum in both the fluid and solid sub-domains as well as continuity:

$$\rho \frac{\mathrm{D}\boldsymbol{v}}{\mathrm{D}t} = \nabla \cdot \boldsymbol{\sigma}^{\mathrm{f}} \quad \boldsymbol{x} \in \Omega^{\mathrm{f}}, \tag{1}$$

$$\rho \frac{\mathrm{D}\boldsymbol{v}}{\mathrm{D}t} = \nabla \cdot \boldsymbol{\sigma}^{\mathrm{s}} \quad \boldsymbol{x} \in \Omega^{\mathrm{s}}, \tag{2}$$

$$\nabla \cdot \boldsymbol{v} = 0 \quad \boldsymbol{x} \in \Omega. \tag{3}$$

We have defined the stress in the solid and fluid to be $\boldsymbol{\sigma}^{\mathrm{s}}$ and $\boldsymbol{\sigma}^{\mathrm{f}}$ respectively. At the boundary of contact between the solid and the liquid we also require a stress balance to be satisfied. In the case of a swimming body, there can be an additional active traction applied at the surface of the particle generated by the internal mechanics of the swimmer. We call this extra active traction $\boldsymbol{f}^{\mathrm{act}}$. We denote this boundary as $\partial\Omega^{\mathrm{s}}$ with an outwardly-pointing unit normal $\boldsymbol{n}$. We write the stress balance condition as

$$(\boldsymbol{\sigma}^{\mathrm{s}} - \boldsymbol{\sigma}^{\mathrm{f}}) \cdot \boldsymbol{n} + \boldsymbol{f}^{\mathrm{act}} = 0 \quad \boldsymbol{x} \in \partial\Omega^{\mathrm{s}}. \tag{4}$$

Two distinct ways of modeling a swimming organism will be presented. While modeling *C. elegans*, we will assume that we know the shapes that the organism forms as a function of time. This will allow us to generate active forces through the solid stress by updating the reference configuration of the swimmer. These input shapes will be provided from direct experimental measurements[23]. In this case the constitutive model will drive the swimmer to the correct shape under the condition that the shear modulus of the swimmer is sufficiently high (meaning any effects of the elasticity of the swimmer are lost, since the only role of the "elasticity" in this case is to drive the swimmer to the correct target shape). In the shape-driven model, we do not need to specify any additional active tractions. This model can be thought of as being shape-controlled (i.e. swim stroke controlled), where speed is a consequence of configuration. One may think of this method as a three-dimensional extension of previous work in two-dimensions where the prescribed "active force" was proportional to the instantaneous deviation from a target curvature of the swimming body (modeled as a infinitesimally thin line)[32,33,35,47]. The second way we will model swimming motion is by directly enforcing an additional active traction $\boldsymbol{f}^{\mathrm{act}}$. This will be our methodology for the amoeboid motion presented later in this paper. In this case the shapes of the swimmers are a direct consequence of the imposed force distribution (and thus are not necessarily the same if we change the fluid properties). Additionally, by using this methodology the elastic properties of the swimming body itself can be incorporated in a meaningful way[46].

Since microorganisms operate in the limit of zero Reynolds number (negligible inertia)[16], conservation of momentum applied to the swimming body requires that any imposed active tractions cannot give rise to a net force or torque:[17]

$$\int_{\partial\Omega^{\mathrm{s}}} \boldsymbol{f}^{\mathrm{act}} dS = 0, \tag{5}$$

$$\int_{\partial\Omega^{\mathrm{s}}} \boldsymbol{x} \times \boldsymbol{f}^{\mathrm{act}} dS = 0. \tag{6}$$

To model a viscoelastic, polymeric suspending medium, we represent the suspending fluid stress as a sum of a Newtonian stress with an additional polymeric stress,

$$\boldsymbol{\sigma}^{\mathrm{f}} = \boldsymbol{\sigma}^{\mathrm{N}} + \boldsymbol{\sigma}^{\mathrm{P}} = -p\mathbf{I} + \eta\left(\frac{\partial \boldsymbol{v}}{\partial \boldsymbol{x}} + \frac{\partial \boldsymbol{v}}{\partial \boldsymbol{x}}^{\mathrm{T}}\right) + \boldsymbol{\sigma}^{\mathrm{P}}. \tag{7}$$

In the above, we have defined p to be the hydrodynamic pressure and η to be the Newtonian fluid viscosity. We describe the extra polymer stress, $\boldsymbol{\sigma}^{\mathrm{P}}$, generally using the Giesekus model[48], which describes the evolution of the extra stress through a conformation

View Article Online
DOI: 10.1039/C8SM02518E

tensor $\mathbf{c}$ and a relaxation time λ,

$$\boldsymbol{\sigma}^{\mathrm{P}} = \frac{\eta_p}{\lambda}(\mathbf{c}-\mathbf{I}), \tag{8}$$

$$\lambda \overset{\triangledown}{\mathbf{c}} + (\mathbf{c}-\mathbf{I}) + \alpha(\mathbf{c}-\mathbf{I})^2 = 0. \tag{9}$$

In Eqn. 9, $\overset{\triangledown}{\mathbf{c}}$ is the upper-convected time derivative and we have defined η_p to be the polymeric viscosity. The Giesekus constitutive equation considers the individual polymer molecules to be Hookean dumbbells, allowing for anisotropic drag via the Giesekus mobility parameter α. The Oldroyd-B model is recovered from the Giesekus model if $\alpha = 0$, and for the majority of this paper the Oldroyd-B model will be considered. The Oldroyd-B model, however, displays no shear thinning, so when we examine both the effects of fluid elasticity and shear thinning on the swimming speed we will utilize the Giesekus model. Otherwise, using the Oldroyd-B model is advantageous as we ensure that the trends we observe are solely elastic in origin. The zero shear viscosity of the suspending fluid is constant and is given by:

$$\eta_0 = \eta + \eta_p. \tag{10}$$

We also must specify a constitutive model for the swimming body. The suspended swimmer will either be modeled as a 3D solid hyper-elastic material or as a 2D hyper-elastic membrane. The second Piola-Kirchhoff stress, $\mathbf{S}$, is calculated using the principle of virtual work from the strain energy density W, which is a function of the invariants of the right Cauchy-Green tensor $\mathbf{C} = \mathbf{F}^{\mathrm{T}}\mathbf{F}$:

$$\mathbf{S} = 2\frac{\partial W}{\partial \mathbf{C}} = 2\left\{\left(\frac{\partial W}{\partial I_1^C} + I_1^C\frac{\partial W}{\partial I_2^C}\right)\mathbf{I} - \mathbf{C}\frac{\partial W}{\partial I_2^C} + I_3^C\mathbf{C}^{-1}\frac{\partial W}{\partial I_3^C}\right\}. \tag{11}$$

For the deformable solid implementation we utilize a slightly compressible neo-Hookean model with bulk modulus λ_p and shear modulus μ_p. The form of the strain energy density W is thus:

$$W = \frac{\lambda_p}{4}(I_3^C - 1) - \left(\frac{\lambda_p}{2} + \mu_p\right)\ln\left(I_3^C\right)^{1/2} + \frac{\mu_p}{2}\left(I_1^C - 3\right). \tag{12}$$

Any membrane in our simulations is assumed to be infinitely thin and therefore we consider a two-dimensional hyper-elastic material model. In this reduced system, we now solve for tensions that have an energy areal density (these tensions obey the same relationships as their stress counterparts but are now denoted with a hat). $I_1^{\hat{C}}$ and $I_2^{\hat{C}}$ are the only two independent invariants of $\hat{\mathbf{C}}$ in this reduced system and the following relationship now holds:

$$\hat{\mathbf{S}} = 2\frac{\partial \hat{W}}{\partial \hat{\mathbf{C}}} = 2\left\{\frac{\partial \hat{W}}{\partial I_1^{\hat{C}}}\mathbf{I} + J^2\hat{\mathbf{C}}^{-1}\frac{\partial \hat{W}}{\partial I_2^{\hat{C}}}\right\}. \tag{13}$$

For swimmers modeled as membranes, the well-known Skalak model is used:

$$\hat{W} = \frac{\hat{\mu}_p}{2}\left(\frac{1}{2}I_1^2 + I_1 - I_2\right) + \frac{\hat{\mu}_D}{8}I_2^2. \tag{14}$$

where $I_1 = I_1^{\hat{C}} - 2$ and $I_2 = I_2^{\hat{C}} - 1$ are the two invariants of the Skalak model. The Skalak model is generally used to enforce local area-incompressibility in a membrane so the dilatational modulus, $\hat{\mu}_D$, is set to be much larger than the shear modulus, $\hat{\mu}_p$.

2.2 Numerical Implementation

To solve the coupled fluid-solid problem we utilize an Immersed Finite Element Method (IFEM). More details about this method can be found in a recent publication[49]. To arrive at the governing equations, we rewrite Eqns. 1 and 2 as a single equation over the total domain as follows:

$$\rho\frac{\mathrm{D}\boldsymbol{v}}{\mathrm{D}t} = \nabla\cdot\boldsymbol{\sigma}^{\mathrm{f}} + \boldsymbol{f}^{\mathrm{IB}} \quad \boldsymbol{x}\in\Omega, \tag{15}$$

where $\boldsymbol{f}^{\mathrm{IB}}$ is the immersed boundary force density. It is clear that for conservation of momentum to be satisfied everywhere, the immersed boundary force density must take the following form:

$$\boldsymbol{f}^{\mathrm{IB}} = \nabla\cdot(\boldsymbol{\sigma}^{\mathrm{s}} - \boldsymbol{\sigma}^{\mathrm{f}}) \quad \boldsymbol{x}\in\Omega^{\mathrm{s}}. \tag{16}$$

The discretized immersed boundary method utilizes two separate grids. The Lagrangian grid tracks the swimmers (Ω^{s}) while a second fixed Eulerian grid is utilized for the entire domain ($\Omega^{\mathrm{s}} + \Omega^{\mathrm{f}} = \Omega$).

We distinguish between the immersed boundary force on the Lagrangian grid and the immersed boundary force in the Eulerian domain which are defined to be $\boldsymbol{F}^{\mathrm{IB,s}}$ and $\boldsymbol{F}^{\mathrm{IB,f}}$ respectively (note that force densities are given by a lowercase $\boldsymbol{f}$ and forces are given by an uppercase $\boldsymbol{F}$).

On the Eulerian domain we therefore solve the following expression with a third order accurate finite volume scheme developed at Stanford's Center for Turbulence research[50]:

$$\rho\frac{\mathrm{D}\boldsymbol{v}}{\mathrm{D}t} = \nabla\cdot\boldsymbol{\sigma}^{\mathrm{f}} + \boldsymbol{f}^{\mathrm{IB,f}} \quad \boldsymbol{x}\in\Omega. \tag{17}$$

We solve for the conformation tensor $\mathbf{c}$ as six scalar equations (since $\mathbf{c}$ is symmetric) using a log-conformation method to ensure positive definiteness[51,52]. Details about this method can be found in previous papers[53–55].

We are left to determine the values of $\boldsymbol{F}^{\mathrm{IB,s}}$ for which we utilize finite elements. Details of this expression can be found in a more detailed computational methods paper published elsewhere[49]. Discretely we can calculate the immersed boundary force at each node in our Lagrangian domain from the First Piola-Kirchoff stress P_{ij} on each element, the shape function at each node N_k, and the extra active tractions $\boldsymbol{f}^{\mathrm{act}}$:

$$F_{k,i}^{\mathrm{IB,s}} = -\int_{\Omega_0^{\mathrm{s}}}\left(P_{ij}^{\mathrm{s}} - P_{ij}^{\mathrm{f}}\right)\nabla_j N_k \mathrm{d}\Omega + \int_{\partial\Omega_0^{\mathrm{s}}}\boldsymbol{f}^{\mathrm{act}}\mathrm{d}S. \tag{18}$$

In the case of a membrane with vanishingly small thickness, we can rewrite the volume integral as an integral over an area. The fluid stresses integrated over a vanishingly small volume go to zero, simplifying our expression. Our discretized local surface now has a coordinate system with two tangent basis vectors $\mathbf{e}_l$, shape functions $\hat{N}_k$ parameterized in the surface coordinate, and a tension $\hat{\mathbf{P}}$. This gives us a force contribution at each node:

View Article Online
DOI: 10.1039/C8SM02518E

$$F^{\mathrm{IB}}_{k,i} = -\int_{\partial\Omega^{\mathrm{s}}_0} \left(\hat{P}^{\mathrm{s}}_{lj}\right) \nabla_j \hat{N}_k e_{l,i} + \boldsymbol{f}^{\mathrm{act}} \mathrm{d}S. \tag{19}$$

Note that in the above expression the gradient of the shape function $\hat{N}_k$ is with respect to the local surface coordinate in the direction of $\mathbf{e}_l$ and $\hat{\mathbf{P}}$ is the tension so l and j in the above expression range from 1 to 2 instead of 1 to 3 as in the previous expressions.

For the solution of Eqn. 17 we require the immersed boundary force on the Eulerian domain, $\boldsymbol{F}^{\mathrm{IB,f}}$. These forces are found discretely through an interpolation operator that spreads the forces $\boldsymbol{F}^{\mathrm{IB,s}}$ to the Eulerian grid[49]. Similarly, a reverse procedure is required to interpolate velocities from the Eulerian Grid back to the Lagrangian Grid so that the position of the swimmer may be updated at each timestep.

2.3 Additional Considerations for Swimmers Modeled as Membranes

Membrane immersed boundary models have two notable special considerations. First, the viscosity of the fluid inside the membrane may not be the same as the exterior fluid and the viscoelastic properties of the fluid inside may need to be neglected. The second important consideration is that the volume of the capsule can drift over time due to interpolation errors, necessitating explicit correction.

For the simulation of swimmers as membranes, we solve the following Poisson equation to determine which nodes of the fluid domain are inside the membrane boundaries (this information is encoded as an indicator function I):

$$\nabla^2 I = \nabla \cdot \mathbf{G}, \tag{20}$$

where

$$\mathbf{G} = \int_{\partial\Omega^{\mathrm{s}}} \mathbf{n} \mathrm{d}S.$$

For details of this implementation see Bagchi *et al.*, 2009[56].

Using this information, the swimmer can be assigned variable viscosity ratios and the viscoelastic part of the stress of the fluid interior to the the membrane can be set to zero (a reasonable assumption if the cytoplasm of a micro-swimmer is negligibly viscoelastic compared to the medium surrounding the swimmer). We can subsequently set the viscosity in the fluid domain to be:

$$\eta_0 = \eta_{\mathrm{out}} + (\eta_{\mathrm{in}} - \eta_{\mathrm{out}})I.$$

We also can set the viscoelastic stress of the fluid inside the membrane to zero by modifying the polymer viscosity (we call this modified polymer viscosity η^*_p):

$$\eta^*_p = \eta_p - \eta_p I.$$

Additionally, since the divergence free character of the flow is not preserved exactly during the velocity interpolation step in the immersed boundary method, the swimmers modeled using a thin membrane may undergo a gradual volume change during the simulation (Note that even though the relative volume change is typically on the order of 10^{-4} and smaller in a single time step, the associated numerical error will propagate and will cause errors of a few percent by the end of the simulation). In order to avoid this, we utilize the volume conservation algorithm proposed by Mendez in 2014[57].

2.4 Modeling the Motion of *C. elegans*

To model the motion of *C. elegans* we extensively use data from experiments to ensure that we are modeling the correct swimming stroke. The data for swim speed reduction and for the shape of the backbone was provided by Paulo Arratia's group, and details about these experiments can be found in numerous papers elsewhere[21,23–25]. In the case of this model, the active tractions are not explicitly specified; instead, the reference configuration of the solid body is updated at every timestep to the desired target shape. If the solid elasticity is sufficiently large then the swimmer will "chase" the desired shape with little error.

We can write all of the governing equations in a standard non-dimensional form for this case as follows (where non-dimensional variables and operators are given an overbar):

$$\mathrm{Re}\frac{\mathrm{D}\bar{\boldsymbol{v}}}{\mathrm{D}\bar{t}} = \bar{\nabla}\cdot\bar{\boldsymbol{\sigma}}^f = -\bar{p} + \beta\bar{\nabla}^2\bar{\boldsymbol{v}} + \frac{1-\beta}{\mathrm{De}}(\mathbf{c}-\mathbf{I}) \quad x\in\Omega^{\mathrm{f}}, \tag{21}$$

$$\mathrm{Re}\frac{\mathrm{D}\bar{\boldsymbol{v}}}{\mathrm{D}\bar{t}} = \frac{1}{\mathrm{Ca}}\bar{\nabla}\cdot\bar{\boldsymbol{\sigma}}^s \quad x\in\Omega^{\mathrm{s}}, \tag{22}$$

$$\bar{\nabla}\cdot\bar{\boldsymbol{v}} = 0 \quad x\in\Omega, \tag{23}$$

$$\mathrm{De}\,\overset{\nabla}{\mathbf{c}} + (\mathbf{c}-\mathbf{I}) + \alpha(\mathbf{c}-\mathbf{I})^2 = 0. \tag{24}$$

We also have the following non-dimensional energy density relationship in the solid:

$$\hat{\bar{W}} = \frac{\lambda_p}{4\mu_p}(I^C_3 - 1) - \left(\frac{\lambda_p}{2\mu_p} + 1\right)\ln\left(I^C_3\right)^{1/2} + \frac{1}{2}\left(I^C_1 - 3\right). \tag{25}$$

We have chosen to non-dimensionalize all of the length quantities with the diameter of the swimmer D_p and all time quantities with the temporal frequency of the swimming motion f ($T = 1/f$ is the period of the swimming cycle). This leaves us with a total of 6 dimensionless parameters: The Reynolds number ($\mathrm{Re} = \frac{\rho f D_p^2}{\eta_0}$), the Deborah Number ($\mathrm{De} = \lambda f$) the viscoelastic viscosity ratio ($\beta = \frac{\eta}{\eta+\eta_p}$), the mobility parameter (α), and the capillary number ($\mathrm{Ca} = \frac{f\eta_0}{\mu_p}$) now appear in the evolution equations. Additionally, $\frac{\lambda_p}{\mu_p}$ appears in the constitutive equation for the solid swimmer.

For the studies presented in this paper the Reynolds number will be smaller than 10^{-1}, but the Deborah number and β will be free to vary. Additionally, we will utilize α to tune how much the suspending solutions shear thin. For most of the paper we will consider the case of zero fluid shear thinning ($\alpha = 0$), but we will briefly consider the effect shear thinning has on undulatory motion. The capillary number in this shape-driven case will actually quantify how well the shape is being "chased" (i.e. how large the forces are that drive the swimmer to the correct configuration) and has no bearing on any measurable elastic properties of the body of the swimming organism. We will therefore set the capillary number to be very small (less than 10^{-5}) so that the shape is adequately followed (any further reduction in capillary number

View Article Online
DOI: 10.1039/C8SM02518E

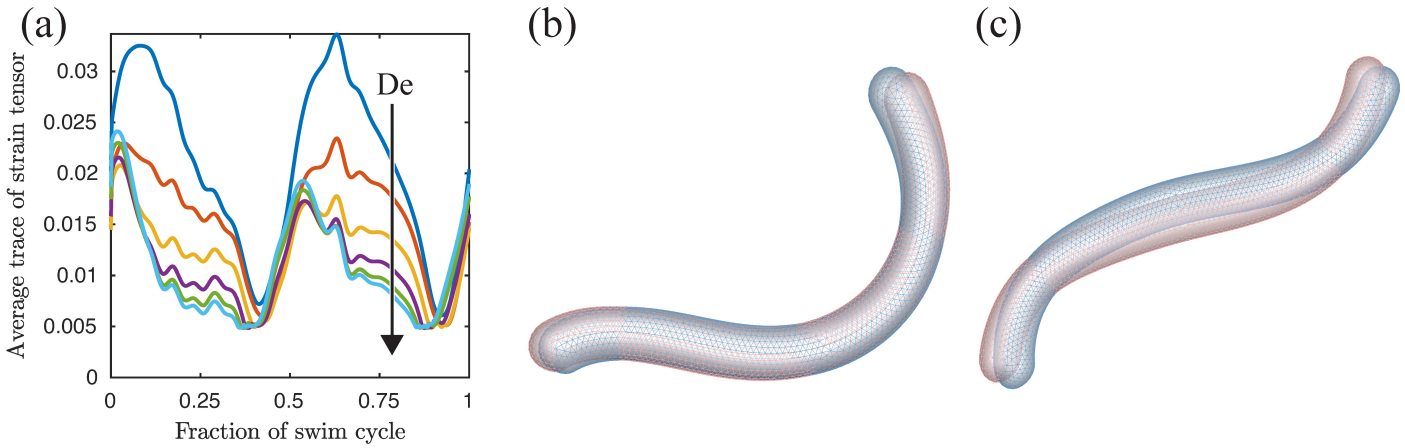

Fig. 1 Analysis of how well the nematode follows prescribed kinematics at very low Ca. a) Steady-state volume averaged trace of the Green-Lagrange strain tensor ($\mathbf{E} = 0.5(\mathbf{F}^T\mathbf{F} - \mathbf{I})$) as a function of time within a swim cycle for a range of De number ($De = 0, 0.1, 0.25, 0.5, 1, 2$) at $\beta = 0.38$. Note that the magnitude of this measure is much less than unity for all presented curves so we are seeing good shape agreement between the actual shape and the prescribed shape. b) The best case scenario for the difference in shapes at the two extreme De numbers of 0.1 (red) and 2 (blue) at $t = 0.5$. c) The worst case scenario for the difference in shapes at the two extreme De numbers of 0.1 (red) and 2 (blue) at $t = 0.6$.

will lead to negligible changes in measured quantities like speed). Additionally, the ratio $\frac{\lambda_p}{\mu_p}$ will be set to be much less than one to ensure that it has no effect on any measured quantities.

In the case of modeling *C. elegans* we are provided with a series of experimental shapes for the backbone of the swimming worm; these snapshots come from the experimental data set utilized in Shen *et al.*[23] Note that as mentioned in that work, the gait of *C. elegans* is largely invariant to changes in fluid elasticity (this is in contrast to other organisms, e.g. *C. reinhardtii*). For this reason, we specify the same set of shapes for both Newtonian and viscoelastic simulations. If at a given timestep we do not have a measured shape, a shape is interpolated in time from the given shapes using cubic spline interpolation. The backbone is a set of coordinates $\boldsymbol{x}_b(s)$ that are parameterized in terms of the arc length of the swimmer, which is assumed to to be of constant length. Additionally this swimmer has a known curvature and tangent vector, $\kappa_b(s)$ and $\boldsymbol{t}(s)$. A spherocylinder mesh of diameter D_p (radius R_p) and length L with points $\bar{\boldsymbol{X}}$ ($0 < \bar{X}_1 < L$ and $0 < \bar{X}_2 < D_p$) is mapped to a new shape for the reference configuration $\boldsymbol{X}$ as follows:

$$X_1 = x_{b,1}(\bar{X}) + t_2(\bar{X}_1)T_p - \chi t_2(\bar{X}_1) \tag{26}$$

$$X_2 = x_{b,2}(\bar{X}) - t_1(\bar{X}_1)T_p + \chi t_1(\bar{X}_1) \tag{27}$$

$$\chi = \left(\frac{1}{\kappa(\bar{X}_1)} + T_p\right) - \frac{1}{2\kappa(\bar{X}_1)}\sqrt{4\left(1 + T_p\kappa(\bar{X}_1)\right)^2 - 8\kappa(\bar{X}_1)\left(\bar{X}_2 - R_p + T_p\right)} \tag{28}$$

$$T_p = \begin{cases} \sqrt{R_p^2 - \bar{X}_1^2}, & \text{if } \bar{X}_1 =< R_p \\ R_p, & \text{if } R_p < \bar{X}_1 =< L - R_p \\ \sqrt{R_p^2 - (\bar{X}_1 - L + R_p)^2}, & \text{if } \bar{X}_1 => L - R_p \end{cases} \tag{29}$$

This shape transformation ensures that the new specified shape conserves volume locally (we are limited to solving for volume incompressible shapes since we use an incompressible flow solver). Additionally, this shape transformation assumes that any motion of the worm maintains that each cross section of the body is normal to the specified backbone. It is worth noting that the transformation presented is not unique and that many different 3D transformations with the same backbone coordinates could be specified. In this case, the transformation proposed is selected because it closely resembles the motions of dorsal and ventral muscles contracting in a real swimming *C. elegans*.

The objective of this method is to study prescribed kinematics where there is little difference in the prescribed shapes depending on the De studied. Therefore, we need to ensure in our simulations that the target shape is actually achieved. In Fig. 1a we examine how well the shape is actually chased for our Ca values of 10^{-5}. We plot the volume average magnitude of the first invariant of the Green-Lagrange strain tensor for multiple De numbers over a cycle. If we were at the prescribed shape we would expect this metric to be exactly zero, and we can see clearly that all values presented are very small compared to unity for all De, meaning that we are prescribing kinematics quite well. In addition, we have shown shape comparison for the lowest and highest De (0.1 and 2) for two different times in the cycle in Fig. 1b/c. At $t = 0.6$ we can see the worst agreement in our strain measures and we see some slight discrepancies in shape. At $t = 0.5$ the strain measures for each De are both small and nearly equal; consequently, we observe shapes that are nearly identical. Therefore, in the studies presented we are studying effects for the case of nearly prescribed kinematics.

2.5 The Amoeboid Model

As a simple model for describing amoeboid motion, we utilize the axisymmetric forcing method first proposed by Farutin and Misbah[43–46]. The swimmer is modeled using a Skalak law membrane

View Article Online
DOI: 10.1039/C8SM02518E

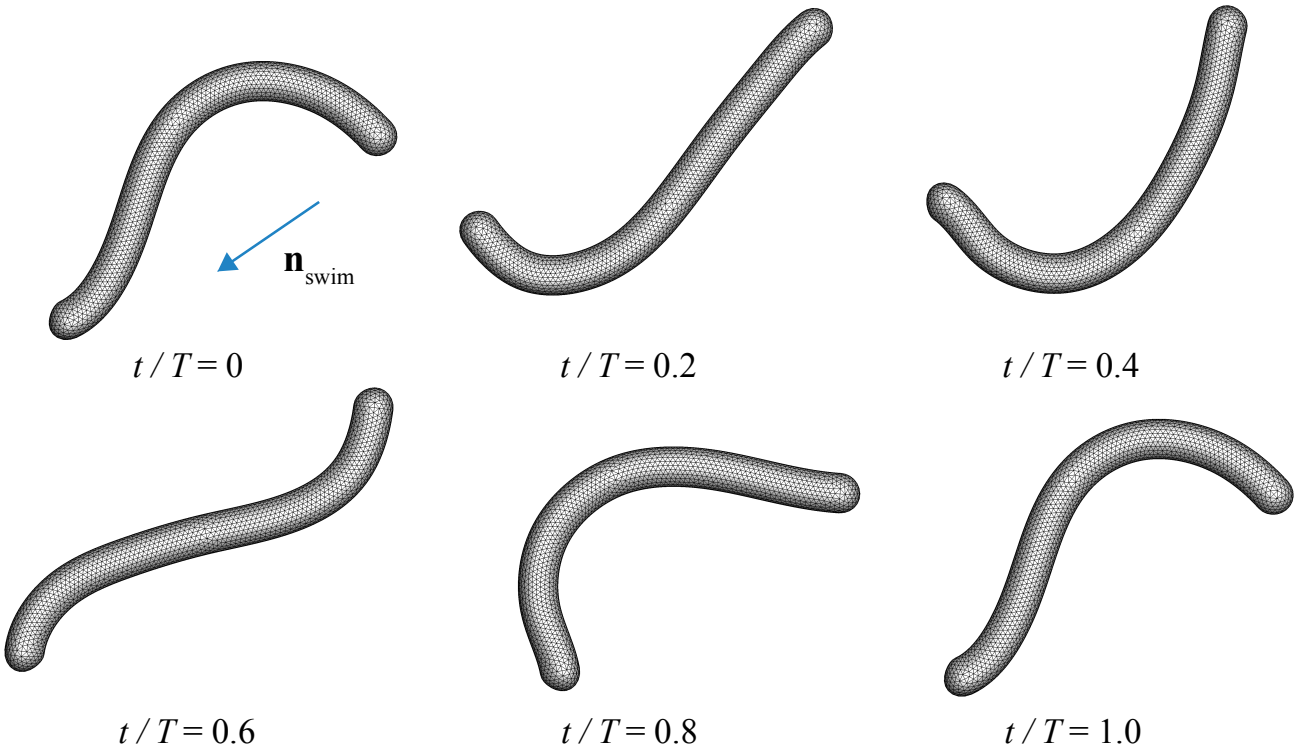

Fig. 2 Shape evolution over time over the course of one period (T) for the *C. elegans* simulations (shown for $\mathrm{De} = 0.1$, $\beta = 0.25$). These shapes are obtained as the computational "elastic" forces are used to drive the nematode towards the prescribed reference configuration. The reference configuration, updated at each time step, is based on experimental measurements provided by David Gagnon and Paulo Arratia of the backbone of swimming *C. elegans* organisms. The arrow denotes the average net swimming direction for the *C. elegans* simulations , $\mathbf{n}_{swim}$. A video of this swimming motion is supplied in the electronic supplementary information †.

with zero shear modulus and a nearly incompressible area with additional active tractions applied to the surface of the swimmer. We start with an initially spheroidal shape and then impose the additional active tractions as follows:

$$\boldsymbol{f}^{\text{act}} = \boldsymbol{n}(\boldsymbol{x}) \sum_{l=2}^{3} F_{l,0} Y_{l,0}(\boldsymbol{X}) + \boldsymbol{F}_1, \tag{30}$$

$$F_{2,0} = F \cos \omega t, \tag{31}$$

$$F_{3,0} = -F \sin \omega t. \tag{32}$$

In the above expression, $Y_{l,m}$ are the spherical harmonics and $\omega = 2\pi f$ is the angular frequency. We only utilize the axisymmetric harmonics in this formulation, but in general more harmonics could be included to generate more complex surface motion. In these expressions $\boldsymbol{x}$ represents the current position of any point of the body in space while $\boldsymbol{X}$ represents the position of the same point in the reference configuration. Since we need our specified forces to introduce no net torque or force, it can be shown that $\boldsymbol{F}_1$ is required to be[46]:

$$\boldsymbol{F}_1 = \boldsymbol{c_1} \times \boldsymbol{n}(\boldsymbol{x}) + \boldsymbol{c_2}, \tag{33}$$

$$\boldsymbol{c_2} = -\frac{1}{A} \int_{\partial \Omega^s} \boldsymbol{f}^{\text{act}} dS, \tag{34}$$

$$\boldsymbol{c_1} = -\frac{1}{2V} \int_{\partial \Omega^s} \boldsymbol{x} \times \boldsymbol{f}^{\text{act}} dS - \frac{1}{2V} \int_{\partial \Omega^s} \boldsymbol{x} \times \boldsymbol{c_2} dS, \tag{35}$$

where A and V are the surface area and volume of the amoeboid respectively.

Similar to the case of the *C. elegans* model, we can write all of the equations in a dimensionless form, where variables have been non-dimensionalized by R_p (the reduced radius of the initial configuration). The evolution equations remain the same as Eqns. 21-24, but the Skalak Law introduces a different non-dimensional energy density:

$$\hat{W} = \frac{1}{2}\left(\frac{1}{2} I_1^2 + I_1 - I_2\right) + \frac{\hat{\mu}_D}{8\hat{\mu}_p} I_2^2. \tag{36}$$

Additionally, the active forces can be non-dimensionalized in the

View Article Online
DOI: 10.1039/C8SM02518E

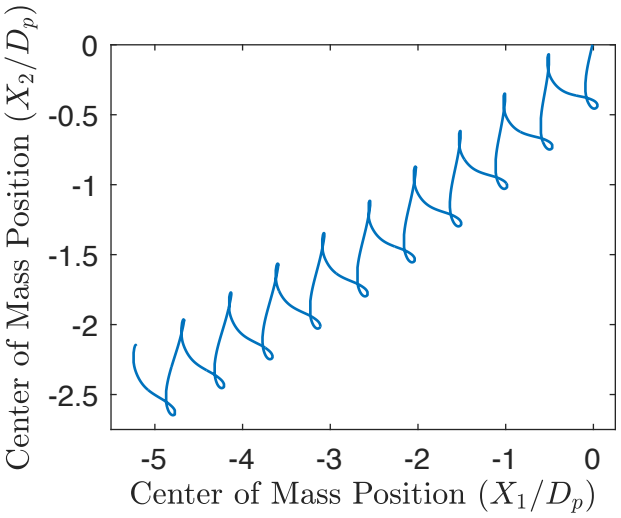

Fig. 3 A sample center of mass trajectory for *C. elegans* in a Newtonian fluid using the same set of shapes illustrated in Fig. 2. Note that the swimmer started in the upper right hand corner of this figure and moved down and to the left. To calculate speed we use the integrated velocity in the average translational direction of this trajectory.

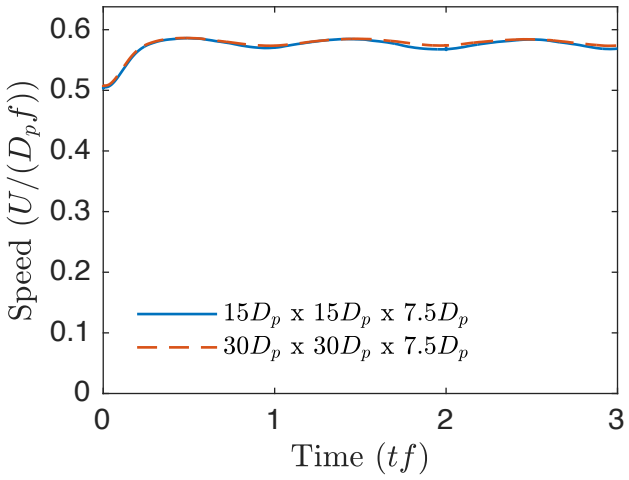

Fig. 4 Speed as a function of time for *C. elegans* in a Newtonian fluid using the same set of shapes that was illustrated in Fig. 2. These two simulations were conducted at two different box sizes. The solid curve is for a box of $15D_p$ x $15D_p$ x $7.5D_p$ and the dashed curve is for a box of size $30D_p$ x $30D_p$ x $7.5D_p$. The maximum difference in these speeds is less than 1%, indicating convergence with respect to box size.

following way:

$$\bar{\boldsymbol{f}}^{\text{act}} = \boldsymbol{n}(\bar{\boldsymbol{X}}) \sum_{l=2}^{3} \bar{F}_{l,0} Y_{l,0}(\bar{\boldsymbol{X}}) + \bar{\boldsymbol{F}}_{\boldsymbol{1}}, \tag{37}$$

$$\bar{F}_{2,0} = S\cos(2\pi\bar{t}), \tag{38}$$

$$\bar{F}_{3,0} = -S\sin(2\pi\bar{t}). \tag{39}$$

This leaves us with a total of 7 dimensionless parameters. As before, the Reynolds number ($\text{Re} = \frac{\rho f R_p^2}{\eta_0}$), the Deborah Number ($\text{De} = \lambda f$) the viscoelastic viscosity ratio ($\beta = \frac{\eta}{\eta+\eta_p}$), and the capillary number ($\text{Ca} = \frac{\omega\eta_0}{R_p\hat{\mu}_p}$) appear in the evolution equations. Additionally, $\frac{\hat{\mu}_D}{\hat{\mu}_p}$ appears in the constitutive equation for the amoeboid swimmer. One additional variable is introduced from the swimming tractions, $S = \frac{F}{\eta_0\omega}$. Lastly, one geometric parameter exists for the initial shape of the spheroidal capsule, which we choose to be the excess area, $\Lambda = \frac{A}{4\pi(3V/4/\pi)^{2/3}} - 1$.

The Reynolds number will be smaller than 10^{-1}, but the Deborah number and β will be free to vary as before. The capillary number in this case will actually quantify the effect of elasticity compared to viscous forces. However in our studies the shear stress in the membrane will be taken to be negligible so that $\text{Ca} = \infty$. The active forcing parameter S quantifies how much extra traction a swimmer can produce relative to the viscous forces in the fluid and will be set to be much greater than 1 in this study. In these studies this ratio is set to 8, and any further increase in this parameter is seen to have negligible impacts on the speed and kinematics of the swimming body. Additionally, the ratio $\frac{\hat{\mu}_D}{FR_p} = (\frac{\hat{\mu}_D}{\hat{\mu}_p})\text{Ca}^{-1}S^{-1}$ will be set to be much greater than one to ensure that our membrane remains nearly area incompressible (as real cells are generally seen to behave this way due to the very limited area-extensibility of the lipid bilayer). In our studies we set this parameter to 64 and note that area is conserved to within 0.5% during a swim cycle.

2.6 Summary of the Numerical Algorithm

The following are the steps in our modified version of the IFEM applied to swimming bodies:

1. Calculate the internal forces on the particle (Lagrangian grid) based on the particle current configuration at time step n, $\boldsymbol{x}_k^{s,n}$, and the reference configuration $\boldsymbol{X}_k^s$, as well as the swimmers velocity $\boldsymbol{v}_k^{s,n}$, and the value of the conformation tensor $\boldsymbol{c}_k^{s,n}$.

   The swimming motion is introduced in this step in one of two ways. When we model *C. elegans* we change the reference configuration, $\boldsymbol{X}_k^s$, according to Eqns. 26-29 and set $\boldsymbol{f}^{\text{act}} = 0$. If we are modeling the amoeboid we calculate $\boldsymbol{f}^{\text{act}}$ using Eqns. 30-32 and the reference configuration is held constant.

   Eqns. 18 and 19 can be utilized to evaluate the immersed boundary forces for a deformable solid like *C. elegans* or for a membrane like the swimming amoeba respectively.

2. Spread the force to the fluid domain (Eulerian grid) at node J, where we represent our spreading/interpolating operator as a series of weights, ϕ. More details about this operator can be found in our previous paper[49].

$$\boldsymbol{F}_J^{\text{IB,f}} = \sum_k \boldsymbol{F}_k^{\text{IB,s}} \phi_J(\boldsymbol{x}_J - \boldsymbol{x}_k^{s,n}). \tag{40}$$

3. Next, the Navier-Stokes and continuity equations are solved to calculate fluid velocities $\boldsymbol{v}$ and pressure p using a finite volume algorithm. The components of the conformation tensor are also updated. As discussed in Sec. 2.2, we utilize a finite volume solver utilizing a fractional step method to

View Article Online
DOI: 10.1039/C8SM02518E

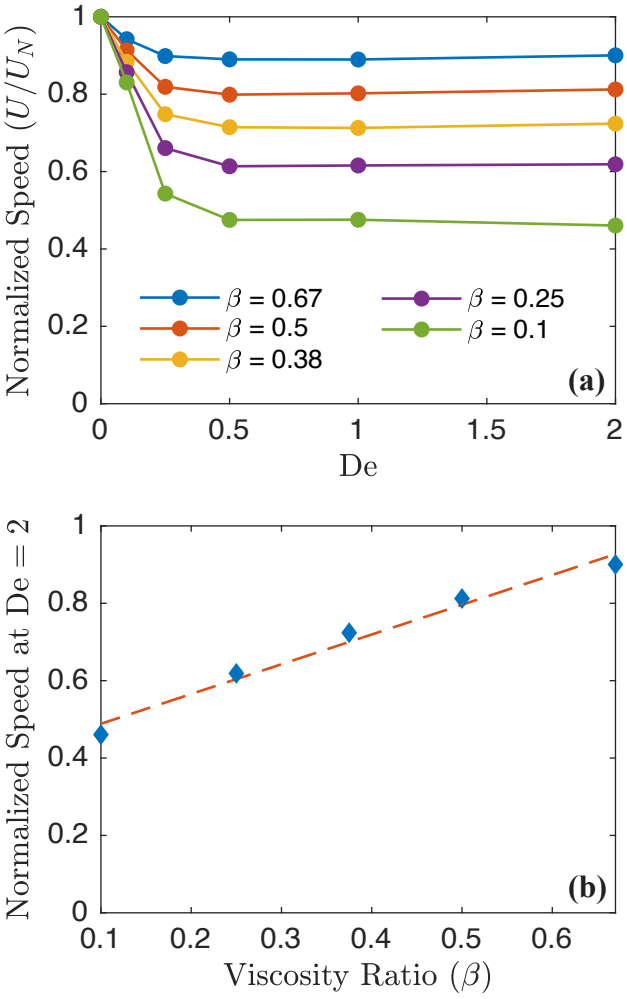

Fig. 5 Average speed (U) normalized by the value in a Newtonian fluid (U_N) for the shape-driven *C. elegans* simulations. For all De and β, the value is less than unity, indicating a swimming speed slower than that in a Newtonian fluid. For large De, the speeds shown in Fig. 52a approach an asymptotic value. These values are plotted as a function of the viscosity ratio, β, in Fig. 52b; the resulting trend suggests that speed reduction scales nearly linearly with β.

solve the Navier-Stokes equations. More details concerning the numerical implementation of this solver, originally developed at Stanford's Center for Turbulence Research, can be found in Ham *et al.* [50]. The viscoelasticity is updated as six scalar equations utilizing a log-conformation method. More details of this algorithm can be found in papers by Richter *et al.* [54] and Yang *et al.* [53].

$$\rho \frac{\mathrm{D}\boldsymbol{v}}{\mathrm{D}t} = \nabla \cdot \boldsymbol{\sigma}^{\mathrm{f}} + \boldsymbol{f}^{\mathrm{IB,f}}, \tag{41a}$$

$$\nabla \cdot \boldsymbol{v} = 0, \tag{41b}$$

$$\lambda \overset{\nabla}{\mathbf{c}} + (\mathbf{c} - \mathbf{I}) + \alpha(\mathbf{c} - \mathbf{I})^2 = 0. \tag{41c}$$

4. Next, the velocities from the Eulerian grid are interpolated back to the Lagrangian grid (to ensure no-slip at the boundary). If we are solving a viscoelastic problem, we also need to know the conformation tensor at each Lagrangian node:

$$\boldsymbol{v}_k^{\mathrm{s},n+1} = \sum_{J \in \text{stencil}} \boldsymbol{v}_J \phi_J(\boldsymbol{x}_J - \boldsymbol{x}_k^{\mathrm{s}}), \tag{42}$$

$$\mathbf{c}_k^{\mathrm{s},n+1} = \sum_{J \in \text{stencil}} \mathbf{c}_J \phi_J(\boldsymbol{x}_J - \boldsymbol{x}_k^{\mathrm{s}}). \tag{43}$$

5. Finally, the Lagrangian grid is updated based on the interpolated velocities using an Adams-Bashforth second-order scheme:

$$\boldsymbol{x}_k^{\mathrm{s},n+1} = \boldsymbol{x}_k^{\mathrm{s},n} + \Delta t\left(\frac{3}{2}\boldsymbol{v}_k^{\mathrm{s},n} - \frac{1}{2}\boldsymbol{v}_k^{\mathrm{s},n-1}\right).$$

In this final step, volume conservation of capsules is strictly enforced.

3 Results and Discussion

3.1 The Effect of Fluid Elasticity on the Swimming Speed of *C. elegans*

With the fully resolved three-dimensional method presented previously, a series of swimming simulations were conducted at constant shape while varying the Deborah number in the Oldroyd-B model. These simulations were conducted in a simulation box of size $15D_p$ x $15D_p$ x $7.5D_p$, where D_p is the diameter of the nematode. The fluid domain is a non-uniform mesh with increasing mesh resolution near the plane of the worm; here, the mesh size is 0.125 x D_p or 0.01 x L where L is the length of the worm. Periodic boundary conditions are used for the boundaries in the x and y direction, while no-slip boundary conditions are utilized for the boundaries in z. These dimensions and boundary conditions in the z direction were chosen so as to emulate the experimental configuration utilized by Shen *et al.*, where the nematodes are swimming in the $x-y$ plane while being confined by plates above and below their plane of motion [23]. The box size in the $x-y$ directions is required to be large enough that the worms are essentially non-interacting. In Fig. 4 we examine the effect of doubling the size of these periodic boundaries. The steady state swimming speed has been changed by less than 1% due to doubling the box size (on the order of other errors we are making in meshing). We see that the effect on the instantaneous speed as a function of time is quite negligible so all simulations presented here will be for a box size of $15D_p$ x $15D_p$ x $7.5D_p$. For this particular set of simulations the backbone shapes used in the method were a series of experimental backbones that were provided by Paulo Arratia's group for *C. elegans*. A single cycle was chosen from this data and was then used to produce periodic motion. The experimental observations show relatively constant kinematics across all tested fluids, so this periodic motion was used in all swimming simulations. In Fig. 2 snapshots of this periodic swimming motion are presented at six different times in the swimming cycle. Note that the swimmer is moving down and to the left as indicated by the blue arrow in Fig. 2a and that the motion is clearly not sinusoidal. A video of this swimming motion is supplied in the electronic supplementary information [†].

To calculate speed the trajectory shown in Fig. 3 is utilized. The center of mass is plotted and the swimmer initially started in

View Article Online
DOI: 10.1039/C8SM02518E

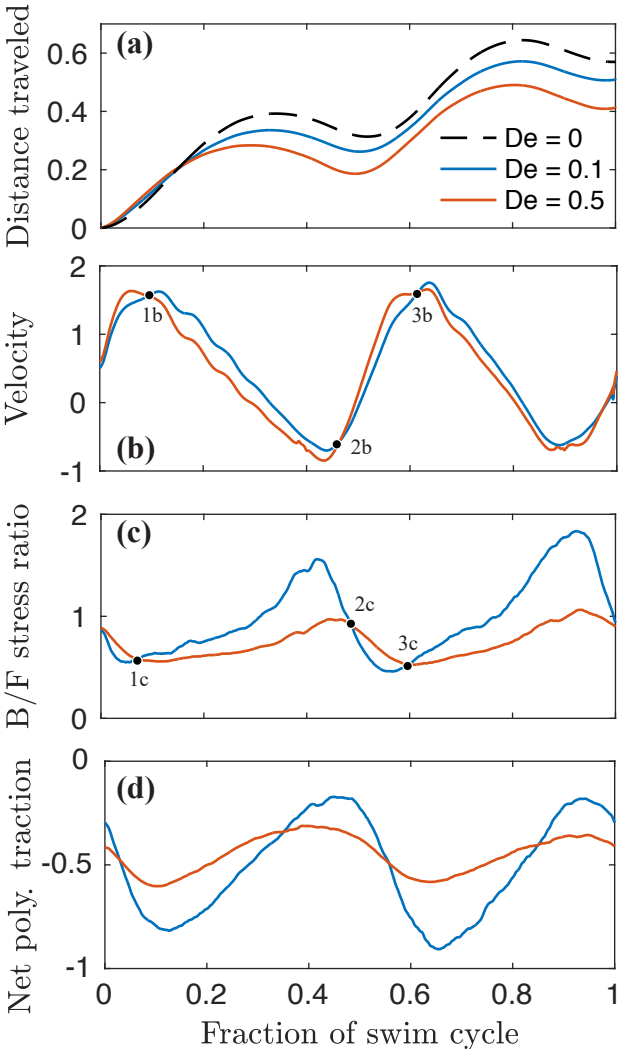

Fig. 6 For $\beta = 0.25$ and De$= 0$, 0.1, and 0.5: a) Net distance the swimmer has traveled in the swimming direction (denoted by $\mathbf{n}_{\text{swim}}$) during a single cycle. b) Slope of Fig. 6a, i.e. the instantaneous velocity in the swim direction. c) Ratio of polymer stress energy integrated over the back half of the worm's surface to that for the front half ($\int_{S_{\text{front}}} \bar{\sigma}^p_{ii} dS / \int_{S_{\text{back}}} \bar{\sigma}^p_{ii} dS$). d) The integrated polymer traction in the swimming direction over the surface of the swimmer $\frac{1}{A}\int_S \bar{\boldsymbol{\sigma}}^p \cdot \mathbf{n} \cdot \mathbf{n}_{\text{swim}} dS$. In this plot, we see a strong correlation between the speed of the worm and the relative integrated stress in front and behind it. For example, up to point 1 in Fig. 6, we see that the De $= 0.1$ simulation exhibits more total stress in the front and swims at a slower speed than that for De $= 0.5$. Past this point we observe a relaxation in stress at the front of the body for De $= 0.1$ and a corresponding increase in speed relative to that of the De $= 0.5$ simulation. We hypothesize that this decreased stress relaxation at the front of the body for the higher De simulations leads to the overall lower swimming speeds seen in Fig. 5. The average polymer traction also correlates very well with the back-to-front ratio of the polymer energy.

the upper right hand corner of the figure and then swam down and to the left (10 cycles are illustrated). To calculate speed we use the component only in the translational direction of motion (down and to the left in Fig. 3). Speed is therefore calculated as (in dimensional units):

$$U = \frac{1}{T}\int_t^{t+T} \mathbf{u} \cdot \mathbf{n}_{\text{swim}} \mathrm{d}t = \frac{|\mathbf{d}(T+t) - \mathbf{d}(t)|}{T} \tag{44}$$

where $\mathbf{n}_{\text{swim}}$ is the unit vector pointing in the direction of the swimming motion and $\mathbf{d}$ is the displacement of the center of mass of the swimmer. The unit vector $\mathbf{n}_{\text{swim}}$ is a constant that points in the net direction traveled over a cycle and is therefore constant over the integration bounds, but isn't necessarily the same for every cycle. Therefore this measure of speed is equivalent to the magnitude of the displacement over a swim cycle divided by the stroke period. Simulations are conducted until a steady swim speed is obtained; this steady state value is utilized in all subsequent analysis.

The results for the simulations with increasing fluid elasticity are presented in Fig. 5. The speed normalized by the speed of a swimmer in a Newtonian fluid decreases as Deborah number increases, and the speed ultimately plateaus at high De. This same observation is made in experimental work by Shen and Arratia[23] as well as in a series of related theoretical model calculations[60]. However, the exact plateau speed is a strong function of β, the ratio of the solvent to total solution viscosity. This feature has been largely unexplored in other computational studies. Moreover the functional behavior in β is not captured well by simple theoretical expressions such as those suggested by Lauga which predicts an ultimate asymptotic speed of zero if the value of $\beta \to 0$[60]. In Fig. 5b we can see that the ultimate plateau that is reached is roughly a linear function of β and the best fit line is drawn as a red dashed curve.

We hypothesize that the reduction in speed is related to strong regions of polymer extension very close to the head and the tail of the swimming *C. elegans*. In Fig. 7 we can see $\bar{\sigma}^p_{ii} = \frac{1-\beta}{\text{De}}(c_{ii} - 3)$ is plotted in three different parts of the swim cycle for two different Deborah numbers of 0.1 and 0.5. Note that all plots of the polymer stress energy $\bar{\sigma}^p_{ii}$ in this study are at the center plane (i.e. $z = 0$). The most notable feature of these contour plots is the extremely high concentration of stress at the head and the tail of the worm. This is notably different than what is observed in many 2D simulations where there is concentrated stress at the head and the tail, but also considerable stress located at other points around the body[32,33,35]. In one 3D simulation of a different organism, *C. reinhardtii*, a similar stress buildup is seen[14] and it appears that the three-dimensional nature of the flow is key to capturing this effect.

At higher De number there appear to be two key effects that drive the worm to swim faster or slower depending on the progress of the worm through its swim cycle. As illustrated in the first and third column of images in Fig. 7, we can see that the ratio of polymer stress in the front of the worm to the back of the worm is larger at higher De which means that there are relatively higher tractions due to the polymer stress acting at the front of the worm (recall that the worm is swimming down and to the left on average during the cycle). The correlation between this stress build-up and slower speed with increasing De allows us to hypothesize that these polymer tractions are causing extra resistance to the worm's motion. This feature increases in magnitude as De increases.

In the second column of images in Fig. 7, we can see extra polymer stress at the back of the worm that is greater in magnitude for low De which likely gives the worm an extra "push" (or

View Article Online
DOI: 10.1039/C8SM02518E

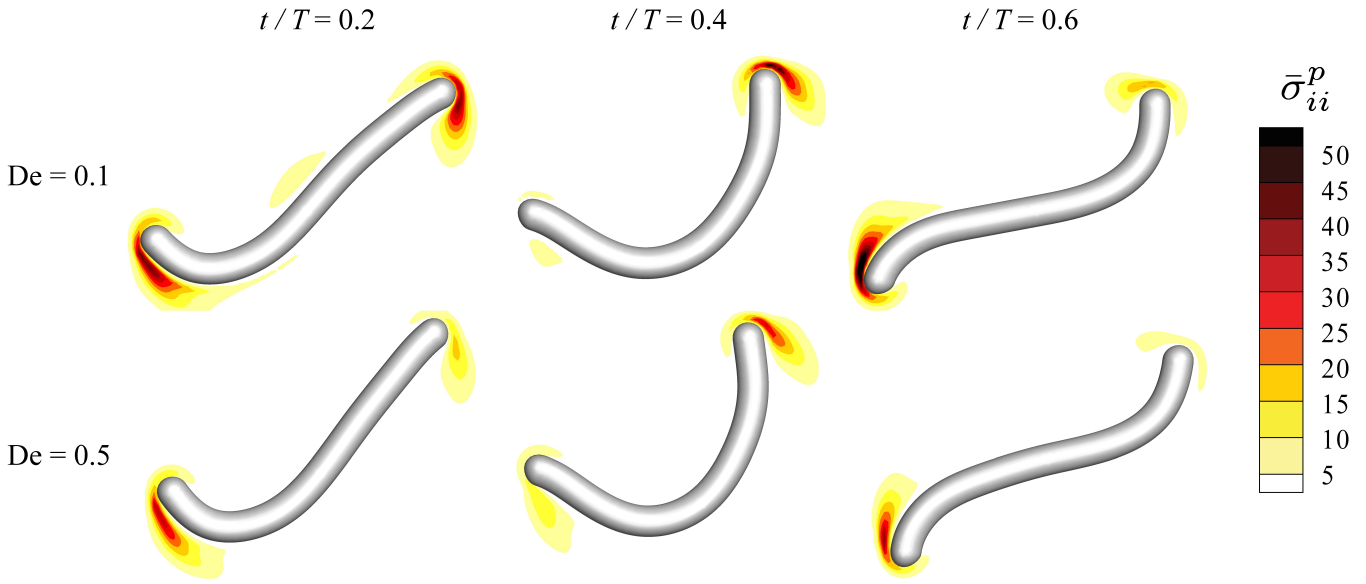

Fig. 7 Polymer stress energy $\bar{\sigma}^p_{ii}$ as a function of De and t for the *C. elegans* simulations at a viscosity ratio of $\beta = 0.25$. In contrast to simulations conducted in 2D, we see that the regions of highest polymer stress are concentrated at the head and tail, rather than around the entire body of the nematode. The contour plots suggest two ways in which *C. elegans* moves more slowly at higher De. First, as illustrated by the set of figures for $t/T = 0.4$, regions of high polymer stress behind the nematode seemingly minimize the degree to which the swimmer "slips" backwards during its swimming motion. Secondly, we observe a slight increase in polymer stress at the head ($t/T = 0.2, 0.6$) in relation to that at the tail of the larger De simulation, suggesting significant resistance to motion at at these points of the swim cycle. All snapshots presented are at the $(z = 0)$ center plane and at steady state.

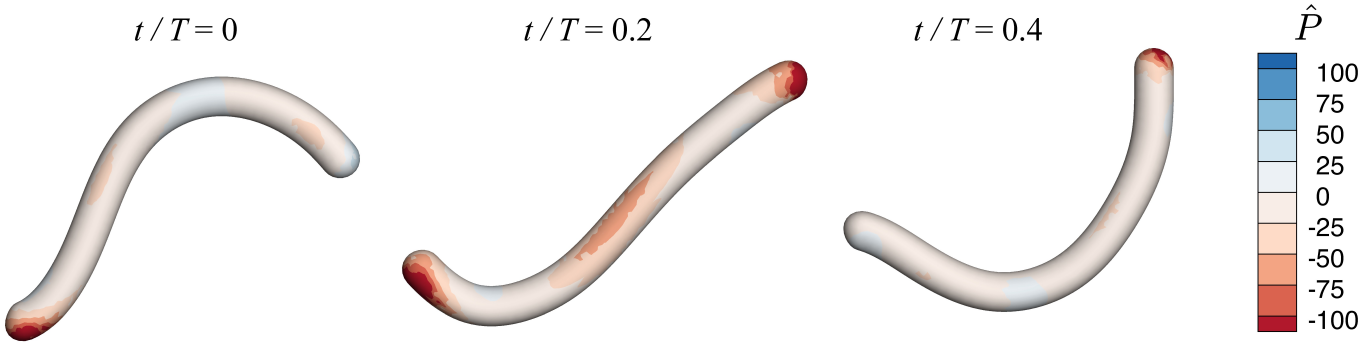

Fig. 8 The local power per unit area exerted on the swimmer by the fluid, $\hat{P} = \bar{\boldsymbol{\sigma}}^p \cdot \mathbf{n} \cdot \bar{\mathbf{v}}$. We see that this power is almost always negative across all of space and time which suggests that the polymer is resisting local motion through the entire cycle. The simulations presented here are at De $= 0.1$ and $\beta = 0.25$. All snapshots presented are at steady state.

at least lower resistance) since extra tractions are now present in the back of the worm due to the polymer stress (an idea similar to that previously offered by Teran *et al.*). We can see in Fig 6b that this time point is when the worm is actually moving backwards, which means that this extra resistance prevents the worm from moving backwards as far as the higher De counterpart. We believe this enhances the speed at low De relative to swimmers at higher De. But, due to the polymer stretch in the regions near the head of the worm, the low De worms still swim slower than their Newtonian counterparts.

In Fig. 6c we have calculated the ratio of the surface integrated trace of the polymer stress tensor (i.e. polymer stress energy) in the front of the worm vs. the back of the worm as a function of time to quantify the previously described hypothesis. We have plotted this alongside the distance traveled in the net swim direction (denoted by $\mathbf{n}_{\text{swim}}$) during the steady state cycle as well as the instantaneous velocity during that cycle in Fig. 6a/b. We can see that the relative value of this stress asymmetry measure for different De simulations correlates with the instantaneous velocities of those simulations. For example, up to point 1c in Fig. 6c, we see that the De $= 0.1$ simulation exhibits a lower stress ratio and swims at a slower speed than that for De $= 0.5$. Past this point we observe an increase in the back-to-front (B/F) stress asymmetry measure and a corresponding increase in speed relative to that of the De $= 0.5$ simulation (see Fig. 6b). From examining Fig. 7 we see that the increase in the back-to-front stress ratio seems to be a result of both relaxation of stress at the front of the body as well as the establishment of more polymer stress behind the

View Article Online
DOI: 10.1039/C8SM02518E

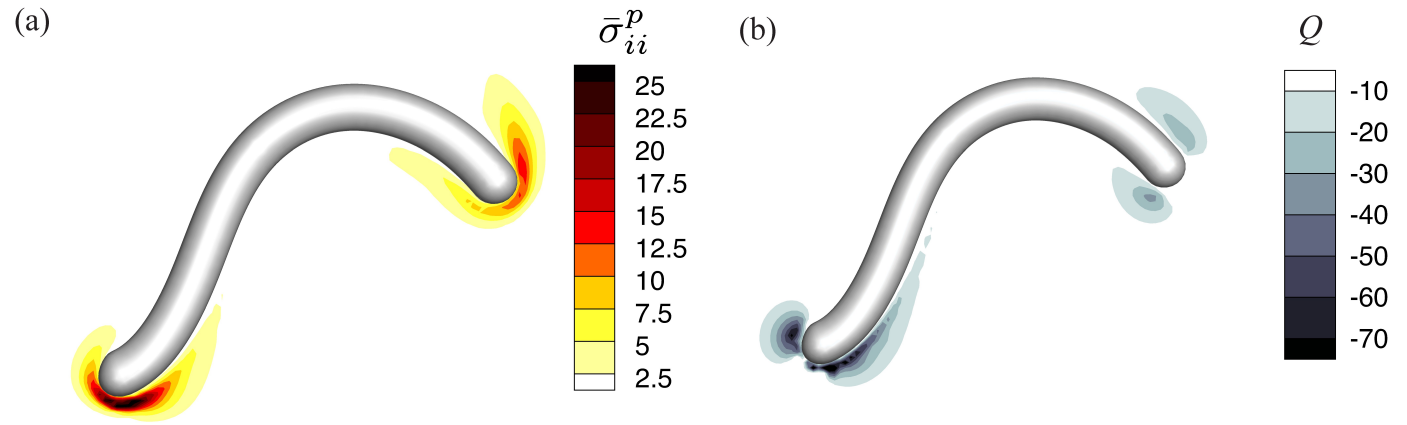

Fig. 9 Polymer stress energy $\bar{\sigma}^p_{ii}$ and the extensional flow strength for the *C. elegans* simulations at $\beta = 0.25$, $\mathrm{De} = 0.1$, $t/T = 1.0$. We use an eigenvalue analysis[58,59] to obtain a qualitative picture of extensional flow around the nematode. To denote the strength of the local extensional flow, we plot the value of $Q = \frac{1}{2}[(\mathrm{tr}(\bar{\nabla}\bar{\mathbf{v}})^2 - \mathrm{tr}(\bar{\nabla}\bar{\mathbf{v}}^2)]$ in the flow field when $D < 0$ since $D = (27/4)R^2 + Q^3 < 0$ denotes regions of extension ($P = -\mathrm{tr}(\bar{\nabla}\bar{\mathbf{v}}) = 0$ for incompressible flow and $R = -\det(\bar{\nabla}\bar{\mathbf{v}})$). We see that the regions of greatest polymer stress are strongly associated with regions of extensional dominated flow; these regions are situated at the head and tail of the nematode. All snapshots presented are at the $(z = 0)$ center plane and at steady state.

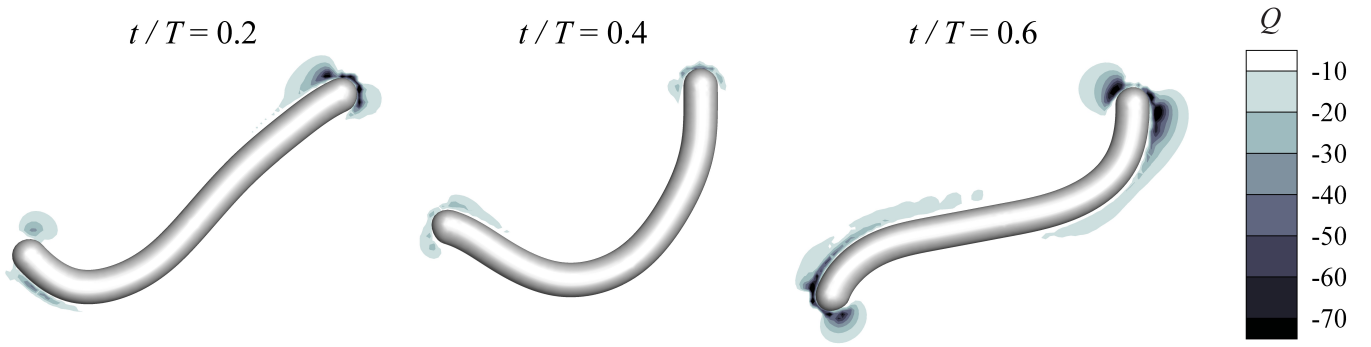

Fig. 10 Extensional flow strength for the *C. elegans* simulations at $\beta = 0.25$, $\mathrm{De} = 0.1$, $t/T = 0.2, 0.4, 0.6$. We use an eigenvalue analysis[58,59] to obtain a qualitative picture of extensional flow around the nematode. To denote the strength of the local extensional flow, we plot the value of $Q = \frac{1}{2}[(\mathrm{tr}(\bar{\nabla}\bar{\mathbf{v}})^2 - \mathrm{tr}(\bar{\nabla}\bar{\mathbf{v}}^2)]$ in the flow field when $D < 0$ since $D = (27/4)R^2 + Q^3 < 0$ denotes regions of extension. We observe extension around the head and the tail at all times during the swimming cycle. All snapshots presented are at the $(z = 0)$ center plane and at steady state.

worm at lower De ($\mathrm{De} = 0.1$). These moments during the swim cycle where the higher De simulations experience lower instantaneous velocities relative to those for smaller De are what give rise to the overall average decrease in swimming speed with respect to De seen in Fig. 5. These moments of lower speed are very clearly correlated with ratio of polymer stretch behind vs. in front of the worm.

In Fig. 6d we have similarly plotted the average polymer traction in the swimming direction on the surface of the worm ($\frac{1}{A}\int_S \bar{\boldsymbol{\sigma}}^p \cdot \mathbf{n} \cdot \mathbf{n}_{\mathrm{swim}} d\mathrm{S}$). This demonstrates our ability to explicitly calculate the polymer tractions (which is a calculation that 2D models cannot perform). It should be noted that the average polymer traction is always resisting the net motion of the swimmer. The average polymer tractions also correlate quite well to the values of the back-to-front polymer energy integral in Fig. 6c. A key feature of this plot is that the lower De swimmer ($\mathrm{De} = 0.1$) has a higher back-to-front ratio and less average polymer traction resistance at the point where the swimmer is moving backwards (near $t/T = 0.4$); this suggests that the extra polymer stretch in the back of the worm seen in Fig. 7 at $t/T = 0.4$ reduces the resistance and helps inhibit the backwards motion of the swimmer.

In Fig. 8 we also have plotted the local power per unit area exerted on the swimmer by the fluid as a function of the position along the swimmer for three different time snapshots. The local power is defined as $\hat{P} = \bar{\boldsymbol{\sigma}}^p \cdot \mathbf{n} \cdot \bar{\mathbf{v}}$. We can see that the polymer traction is almost always resisting the local motion since the power is nearly always negative. This suggests that the role of the polymeric tractions is largely to resist motion, but when the swimmer is moving backwards instantaneously during the cycle (near $t/T = 0.4$ for example) the resistance actually aids in the net motion of the worm since it prevents the swimmer from recoiling substantially.

We use an eigenvalue analysis (which we refer to as PQR analysis) similar to that used by Ooi *et al.* and Terrapon *et al.* [58,59] and first introduced by Chong *et al.* [61] to obtain a qualitative picture of the flow topology around the nematode so as to understand the origin of the stresses seen in Fig. 7. Flow at any point in space can be characterized by the eigenvalues and eigenvectors of the

View Article Online
DOI: 10.1039/C8SM02518E

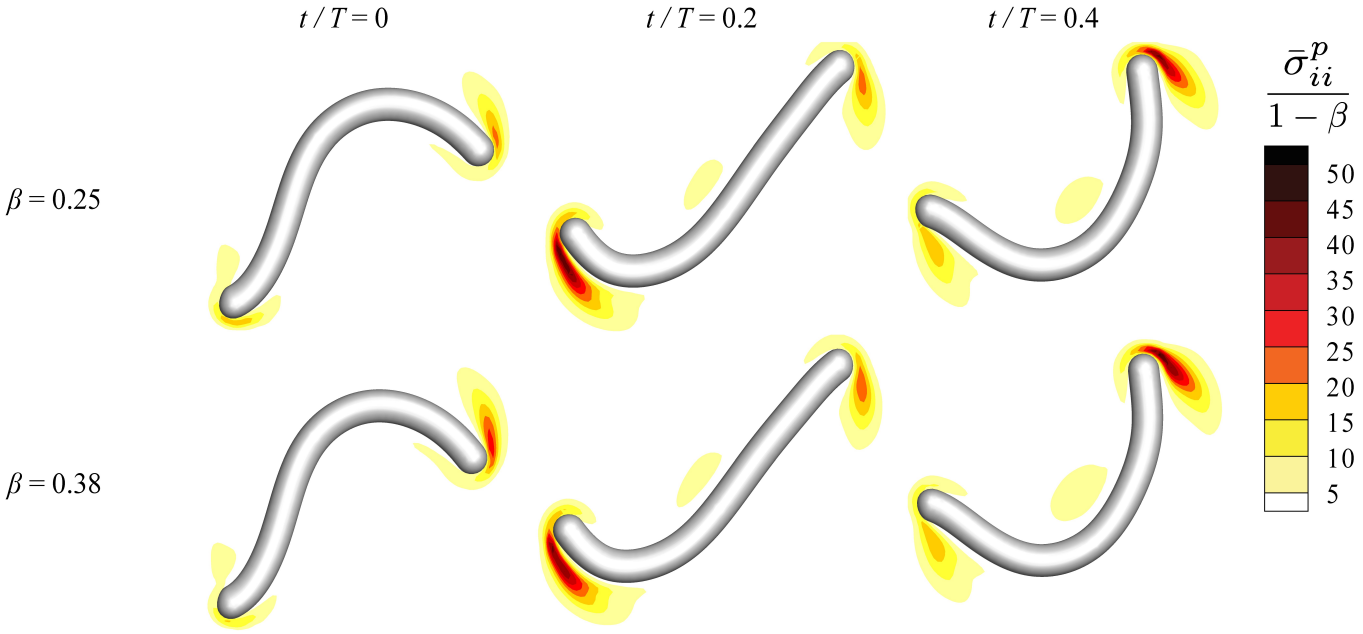

Fig. 11 Polymer stress energy normalized by $(1-\beta)$ (i.e. $\frac{\bar{\sigma}^p_{ii}}{1-\beta}$) as a function of β and t for the *C. elegans* simulations at a Deborah number of $\mathrm{De}=0.5$. As a function of β, we observe only a slight change in the polymer stretch field at various points of the swim cycle. In light of the trend in swim reduction vs. β seen in fig. 5, this suggests that decreasing the viscosity ratio β leads to a slower swimming speed by merely amplifying the effect seen at larger values of β (rather than altering the distribution of stress). All snapshots presented are at the $(z=0)$ center plane and at steady state.

velocity gradient tensor. There are either three real eigenvalues or one real eigenvalue and a complex conjugate pair. If there are three real distinct eigenvalues then the flow is extensional in nature, and in the case of one real eigenvalue the flow is vorticity dominated (i.e. rotational). We can determine which is the case through the values of the invariants of the velocity gradient tensor: $Q=\frac{1}{2}[(\mathrm{tr}(\bar{\nabla}\bar{\mathbf{v}})^2-\mathrm{tr}(\bar{\nabla}\bar{\mathbf{v}}^2)]$ and $R=\det(\bar{\nabla}\bar{\mathbf{v}})$ (the third invariant $P=-\mathrm{tr}(\bar{\nabla}\bar{\mathbf{v}})=0$ for an incompressible fluid). The discriminant, $D=(27/4)R^2+Q^3$, differentiates between regions of extension and those dominated by rotation. If $D<0$, there exists three real distinct eigenvalues at that point in the fluid and is thus a region of predominantly extensional flow. Throughout this document we plot the value of $Q=\frac{1}{2}[(\mathrm{tr}(\bar{\nabla}\bar{\mathbf{v}})^2-\mathrm{tr}(\bar{\nabla}\bar{\mathbf{v}}^2)]$ if $D<0$. As discussed in Terrapon *et al.*, the tensor invariant Q measures the relative rotation and strain of the flow, so that the smaller the value of Q, the stronger the degree of extension[58]. Since all values presented in this work are dimensionless, any value of Q which has a magnitude greater than 1 (and is negative) is to be interpreted as a region of strong extension.

In Fig. 9, we can see that regions of very high polymer extension correspond to the regions in the flow that have the highest extension rates. The right panel shows clearly that the regions of strong extensional flow (large, negative Q) occur near the head and the tail but there is very little extensional flow anywhere along the rest of the worm's body. Additionally in Fig. 10, we can see that the extensional regions are located around the head and tail of the worm for all times and virtually nowhere else. This is in line with the observations of polymer stretch. The difference in the resulting polymer extension as a function of time for differing values of De presented in Fig. 7 can be explained by a history effect. The higher De fluids allow for the polymer to remain extended longer after the extensional flow has relaxed, causing areas of stretch to persist for much longer in the higher De cases. In experimental measurements, areas of extension have been noted considerably far away from the surface of the worm[23]. Those extensional points are present in the simulations as well, but the magnitude of extension at those points is extremely weak compared to the near head and the tail regions, and virtually no polymer stretch is observed in these more distant areas. It is unlikely that these remote points are responsible for any of the observed slowdown.

The nearly linear reduction in speed as a function of β observed in Fig. 5 is very interesting given the very non-linear nature of this problem. To explore this further $\frac{\bar{\sigma}^p_{ii}}{1-\beta}=\frac{1}{\mathrm{De}}(c_{ii}-3)$ in three different parts of the swim cycle for two different β values of 0.25 and 0.38 are shown in Fig. 11. Surprisingly, we observe that the polymer stretch looks virtually identical for these two different values of β. This clearly explains the linear speed reduction as a function of β, since the ultimate stress experienced around the worm due to the polymer is simply $(1-\beta)\,\bar{\sigma}^p_{ij}$. The nearly constant value of $\frac{\bar{\sigma}^p_{ii}}{1-\beta}$ around the worm suggests that the linear β pre-factor then controls the asymptotic slowdown. It would appear that there is an asymptotic value of the swim speed for $\beta\to 0$ that is non-zero (i.e. a non-zero speed in a Maxwell fluid), though we have not tried to simulate this particular fluid.

The final goal of this study is then to compare the results of our simulation to the experimental results of Shen and Arratia[23] and previous numerical results[33]. In Fig. 12 we plot our swim speed data against that of the two aforementioned studies. In the top panel our speed reduction at $\beta=0.67$ is plotted as a solid line

View Article Online
DOI: 10.1039/C8SM02518E

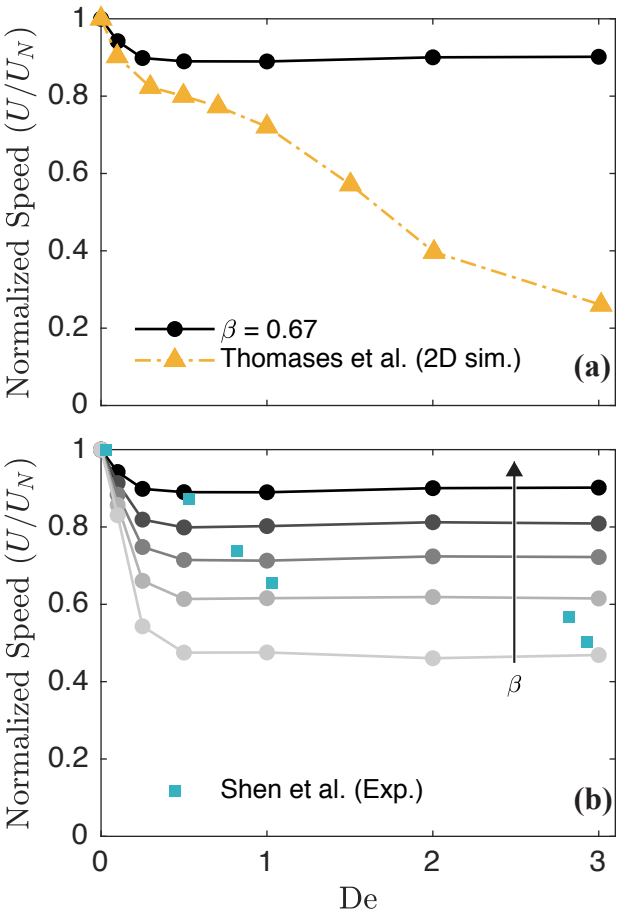

Fig. 12 a) Comparison of normalized average speed (U/U_N) as a function of De to recent 2D simulation[33] and experimental results[23]. We see that 2D simulations (which were also conducted at $\beta = 0.67$) predict a greater speed reduction (lower value of U/U_N) than those in 3D for all De. b) Comparison to experimental data by Shen *et al.*[23]. We see a qualitative agreement in regards to a monotonic decrease in swimming speed to a asymptotic reduction at large De. All β values have been plotted since the experimental data points correspond to different viscoelastic fluids with different values of β.

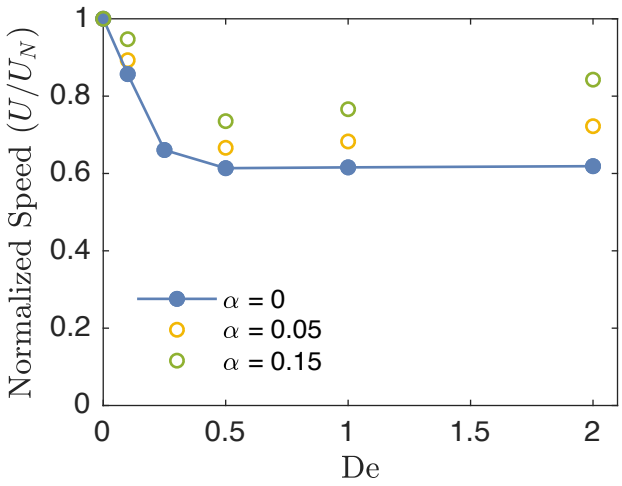

Fig. 13 The simulated speed reduction for *C. elegans* at $\beta = 0.25$ for a series of Deborah numbers compared for two fluids. The solid purple line is the speed reduction for an Oldroyd-B fluid and the open orange and blue symbols are for a Giesekus fluid with $\alpha = 0.05, 0.15$ respectively. The Giesekus model at $\alpha = 0.15$ is highly shear thinning. We see that the overall speed reduction is lowered due to shear thinning and that there is no longer an asymptotic speed reduction.

with circular points against the results of a 2D simulation study by Thomases and Guy for a similar system (the "stiff burrower") as a dashed red line[33]. Notably our speed reduction is much smaller than those observed in 2D across all values of De. This is likely due to the observations made about polymer extension in 3D being highly localized to the head and the tail in Fig. 7. In 2D simulations the stress is much more dispersed around the body, but in the 3D simulations it appears that much of this stress is allowed to relax in the third dimension.

In Fig. 12b we compare our results across a range of β values against the results from Shen and Arratia[23]. The data collected experimentally is at very low $\beta < 0.05$ (evaluated to be $\frac{\eta_w}{\eta_0}$ where η_w is the viscosity of water). We do capture the asymptotic value of speed reduction at low β. However, the results seen by Shen and Arratia are not captured quantitatively over the whole range of De. There are two major reasons that likely account for this difference. First, we assume a very specific 3D motion around the captured experimental 2D backbone adequately describes the entire worm deformation, but in fact there are many such deformations that are consistent with the worm images. Secondly, each data point captured by Arratia is at a different value of β since each solution is a different mixture. A closer evaluation of the fluid rheology for each mixture at each of their data points with more attention to the best fit value of β might lead to a better fit with the experimental data. For example, we can see that since β decreases moving left to right in the experimental data (as more polymer is added to solution), if the best fit values of β for the fluids are higher for the lower De data points, then there would be considerably better agreement in the comparison curves.

Lastly, we probe the effect that shear thinning has on the speed reduction. It has largely been observed experimentally that shear thinning has a very small effect on the swimming kinematics and on the swim speed reduction in non-elastic fluids[23,24]. Additionally, in a theoretical perturbation analysis of Taylor's swimming sheet, the effect of shear-thinning rheology only appears at fourth order in the waving amplitude[62] whereas elastic effects appear at second order[27,63]. In Fig. 13 we see that adding considerable shear thinning to our simulations does quantitatively and qualitatively change the speed reduction behavior as a function of Deborah number. The original results at $\beta = 0.25$ are plotted as a solid curve ($\alpha = 0$) with filled symbols while the Giesekus model results with $\alpha = 0.05, 0.15$ are plotted with open symbols in orange and blue. The Oldroyd-B model (which is simply the Giesekus model with $\alpha = 0$) exhibits no shear thinning. We utilized this model for all of our previous discussions to isolate the effect of fluid elasticity on swim speed without considering shear thinning effects. In contrast, the Giesekus model does exhibit shear thinning, the magnitude of which increases with increasing α. Details concerning the magnitude of this shear thinning in simple shear

View Article Online
DOI: 10.1039/C8SM02518E

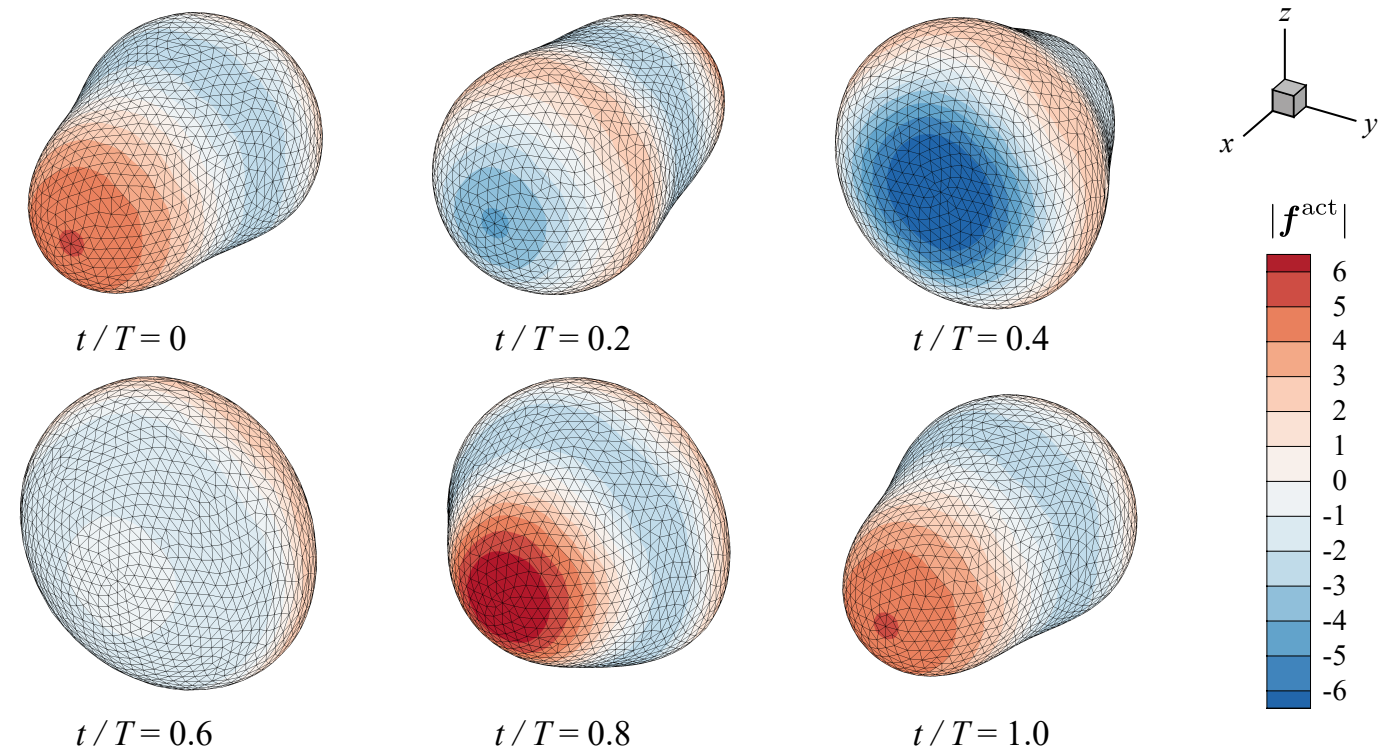

Fig. 14 Example shape evolution for the amoeboid simulations over the course of one period (shown here for $\mathrm{De} = 5$, $\beta = 0.75$). The time signatures indicate the fraction of a full swim cycle at which a given shape is observed. The contour plot denotes the magnitude of the prescribed active traction (force per unit area). A positive value of this active forcing (red) denotes the amoeba's membrane is being extended outward in the normal direction at that point on the surface; a negative value (blue) denotes withdrawal of the membrane surface inward. A video of this swimming motion is supplied in the electronic supplementary information †.

flow as a function of α can be found in the original paper by Giesekus in 1982[64]. The results that we show in Fig. 13 therefore correspond to the non-shear thinning case as a solid line (the Oldroyd-B results) as well as two cases with increasing amounts of shear thinning. The shear thinning introduced by the Giesekus model has two main effects. The speed reduction is generally smaller for the shear thinning model, and the asymptotic speed reduction now shows considerable recovery at high De. Interestingly, this shear thinning effect is qualitatively the same as that predicted by Li *et al.* in their 2D numerical study of Taylor's waving sheet. There, the inclusion of shear thinning behavior in their viscoelastic constitutive model led to a recovery in speed reduction at higher De[13]. These results suggest that the effects of shear thinning and fluid elasticity may interact in non-trivial ways that should be carefully explored experimentally, although this effect appears to be secondary in nature to the effect of elasticity.

3.2 The Effect of Fluid Elasticity on the Swimming Kinematics of Amoeboid Motion

We now examine the effect of fluid elasticity on amoeboid motion. Amoeboid motion is an idealized swimming motion that contrasts that of the worm since the amoeboid swims through purely normal deformation of its surface (in contrast, the worm swims by extension and contraction of its dorsal and ventral muscles). The amoeboid simulations were conducted in a simulation box of size $10R_p$ x $10R_p$ x $10R_p$, where R_p is the reduced radius of the initial configuration ($\Lambda = 0.05$). The fluid domain is a uniform mesh with a mesh size of 0.12 x R_p. Periodic boundary conditions are used for the boundaries in the x direction, while no-slip boundary conditions are utilized for the boundaries in y and z. Note that the axisymmetry of the prescribed forces in the amoeboid model cause it to swim in the positive x direction. The distance of the no-slip boundaries in the lateral directions (y and z) are chosen such that they have a negligible impact on the speed of the swimmer (indeed, the confinement ratio $C = \frac{2R_p}{W}$ as defined by Wu *et al.* is 0.1, indicating a low degree of confinement[45]). Before proceeding with simulations in a viscoelastic fluid, we validated the speed of an amoeba in a Newtonian fluid against the results for Ranganathan *et al.*[46] utilizing their stated parameters. This comparison was done in the context of $\mathrm{Ca} \gg 1$ to rule out differences in solid constitutive models as a source of error. We found that our speed was within 2% of the speed reported in this work allowing us to be confident that our algorithm was implemented correctly. Below in Fig. 14 we have illustrated six snap-shots of the amoeboid moving in different parts of the cycle. A video of this swimming motion is supplied in the electronic supplementary information †. The contours illustrated on the surface are the magnitude of the extra active traction which is presented in Eqn. 14.

A series of simulations were conducted varying De utilizing the Oldroyd-B model while maintaining an internal viscosity equal to

View Article Online
DOI: 10.1039/C8SM02518E

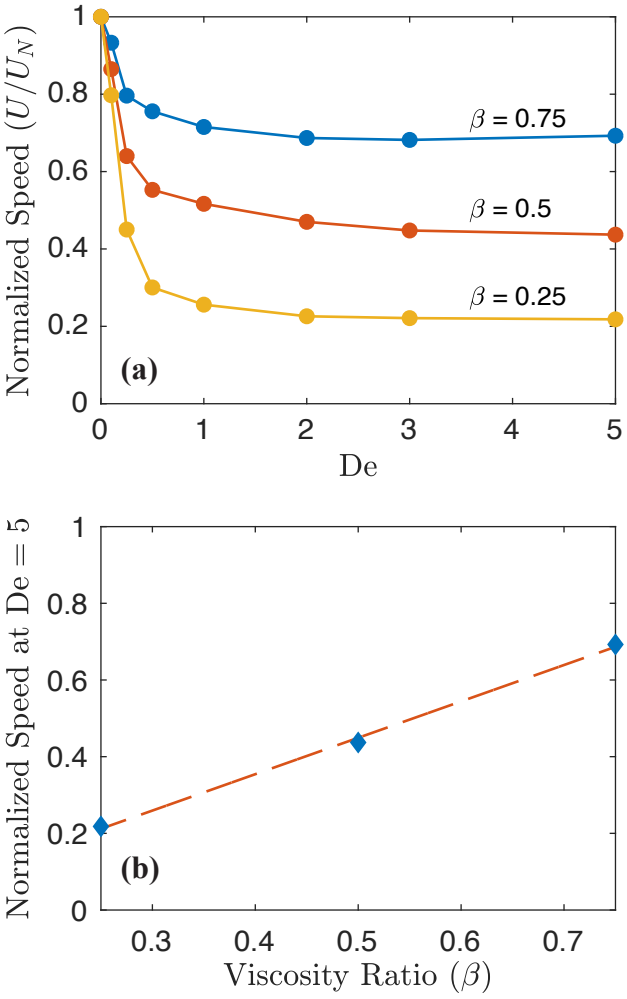

Fig. 15 Normalized average speed (U/U_N) for the amoeboid simulations. Similar to the results for the *C. elegans* simulations, we observe a monotonic decrease in swimming speed to an asymptotic value for large De. In contrast, however, the speed reduction for the amoeba is always greater than that for the *C. elegans* simulations at the same value of β. The asymptotic values are plotted as a function of the viscosity ratio, β, in Fig. 15b; as we saw for the *C. elegans* simulations, the speed reduction scales nearly linearly with β.

the external viscosity with no polymer contribution. In Fig. 15, where we plot the normalized speeds, we see many similar features to the same plot for *C. elegans* (Fig. 5). In Fig. 15 we note that there is an ultimate speed reduction observed at high De and that there is always a slowdown observed in all cases. However, the ultimate asymptotic speed reduction for the amoeboid swimming motion is more severe at low values of β relative to that of *C. elegans*. In Fig. 16 we note that the polymer stretch is not isolated to small regions of the body (like the head and the tail for *C. elegans*) and instead appears to accumulate everywhere around the amoeboid surface in a thin layer.

In Fig. 16 we can see some similarities between the polymer stress energy for the *C. elegans* simulations and the amoeboid simulations. The polymer stress energy, $\bar{\sigma}^p_{ii} = \frac{1-\beta}{\mathrm{De}}(c_{ii}-3)$ is plotted for the amoeboid simulations for $\mathrm{De} = 0.25$ and $\mathrm{De} = 5$ at a three time points in a swimming cycle. In both cases there are extreme areas of polymer stress that accumulate near the body of the swimmer in a thin boundary layer. However, in the case of the amoeboid, stress accumulates everywhere around the body of the swimmer instead of being isolated around the head and the tail. As the amoeboid swims there are areas of extensional flow that appear around the swimmer and at high De the resulting areas of stretched polymer are never allowed to relax due to the finite relaxation of the polymer and the recurring areas of extension (in contrast the undulatory motion of *C. elegans* creates extensional flow that is concentrated in very small regions near the head and tail).

As a function of β, the asymptotic reduction in swim speed again shows similar behavior to that of *C. elegans* where it appears to nearly linearly depend on β in Fig. 15b. In Fig. 17 we see that the polymer stretch near the amoeba ($\frac{\bar{\sigma}^p_{ii}}{1-\beta}$) looks remarkably similar for two different values of β. In this case we note that there is a small amount of difference between the contours, especially in the frame at $t/T = 0.6$, which likely explains the slight non-linear behavior we observe in the asymptotic speed reduction as a function of β. The similarities between the phenomena of stress accumulation in thin boundary layers and the ultimate speed reduction dependence on β for *C. elegans* and the amoeboid in viscoelastic fluids are remarkable given the very different modes of motion and swim strokes. It is also notable that the two different ways that we can simulate motion (either with constant swim stroke or by a fixed extra active traction) seem to produce a very consistent qualitative trend regarding the reduction in swim speed.

However, when examining the regions of extensional flow around the amoeboid in Fig. 18, we can see that unlike *C. elegans*, there is not one single region where extension is prevalent throughout the whole cycle. We use the same PQR analysis we used for the nematodes to characterize the three-dimensional flow field[58,59] to obtain a qualitative picture of extensional flow around the amoeba. We plot the value of $Q = \frac{1}{2}[(\mathrm{tr}(\bar{\nabla}\bar{\mathbf{v}})^2 - \mathrm{tr}(\bar{\nabla}\bar{\mathbf{v}}^2)]$ if $D < 0$ at various times throughout the cycle. We define $D = (27/4)R^2 + Q^3$ and if $D < 0$ we are in a region of extensional flow. Unlike *C. elegans*, areas of extension appear in many places along the surface of the body leading to different areas along the body experiencing the strongest extension during different parts of the cycle. These areas of extension have varying strength, but appear laterally as well as in front/behind the amoeboid depending on the time in the cycle. We hypothesize that the areas of extension combined with the finite relaxation time of the suspended polymers results in the thin boundary layer of polymer extension nearly everywhere around the amoeboid's surface in Fig. 16. It seems the Lagrangian history of each point that tracks with the surface of the swimmer experiences extension at some point during the cycle, but then the associated polymers are unable to relax at sufficiently high De number making the observed boundary layer more disperse than in the case of *C. elegans*. Although the regions of extension appear weaker than those for *C. elegans*, the local De number ($\mathrm{De}_{\mathrm{local}}$) is actually quite high in these extensional regions. In the second row of Fig. 18 the local De number is plotted for the same time snapshots. We have defined the lo-

View Article Online
DOI: 10.1039/C8SM02518E

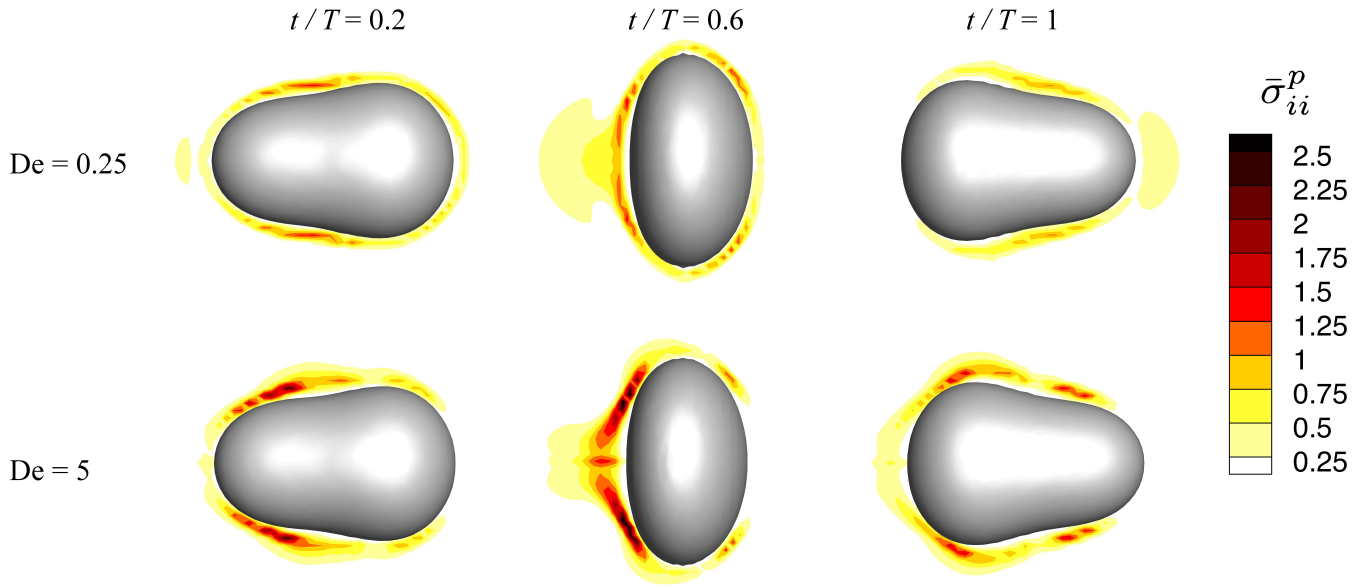

Fig. 16 Polymer stress energy $\bar{\sigma}^p_{ii}$ as a function of De and t/T for the amoeboid simulations at a viscosity ratio of $\beta = 0.25$. We observe an increase in the polymer stress energy with De at all moments during the swim cycle. We note that this is qualitatively different from what is observed in the *C. elegans* simulations, where for example at $t/T = 0.2$ it appears that the average polymer extension is greater at lower De. This suggests that the mechanism for the amoeboid speed reduction is somewhat different than that for *C. elegans*, although both involve a thin boundary layer of polymer extension. We hypothesize that the speed reduction for the amoeba is related to the fact that, due to its axisymmetric beating pattern, it swims in a straight line and thereby accumulates polymeric stress around the entirety of its body. All snapshots presented are at the $(z = 0)$ center plane and at steady state.

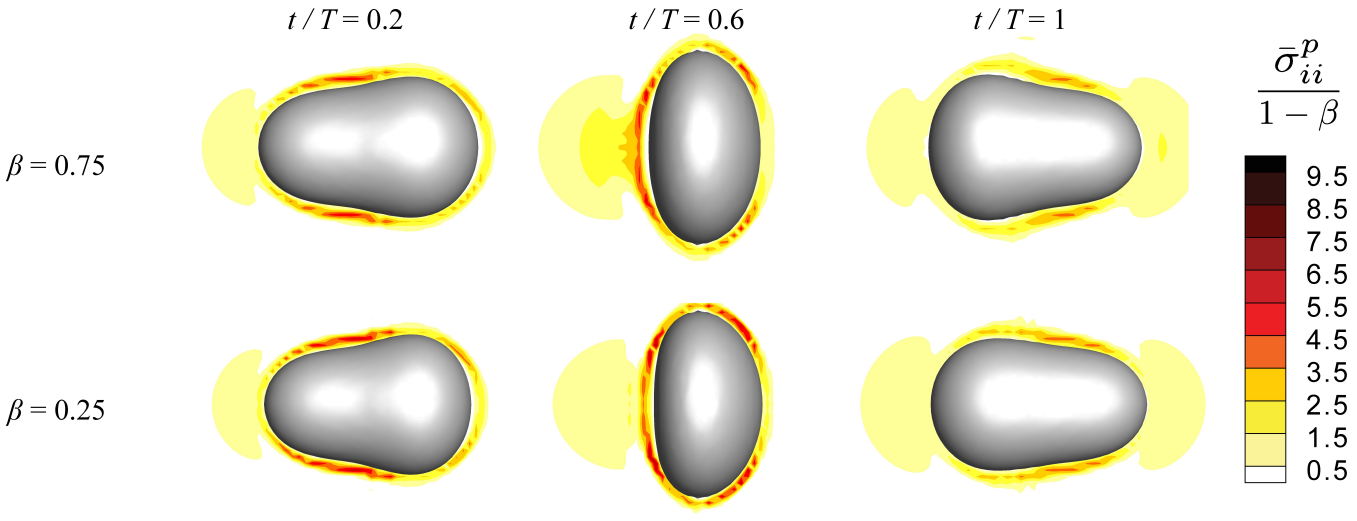

Fig. 17 Polymer stretch $\frac{\bar{\sigma}^p_{ii}}{1-\beta}$ as a function of β and t/T for the amoeboid simulations at De $= 0.25$. Note that there are only very subtle changes as a function of β, but small differences can be seen near the right side of the amoeboid at $t/T = 0.6$. All snapshots presented are at the $(z = 0)$ center plane and at steady state.

View Article Online
DOI: 10.1039/C8SM02518E

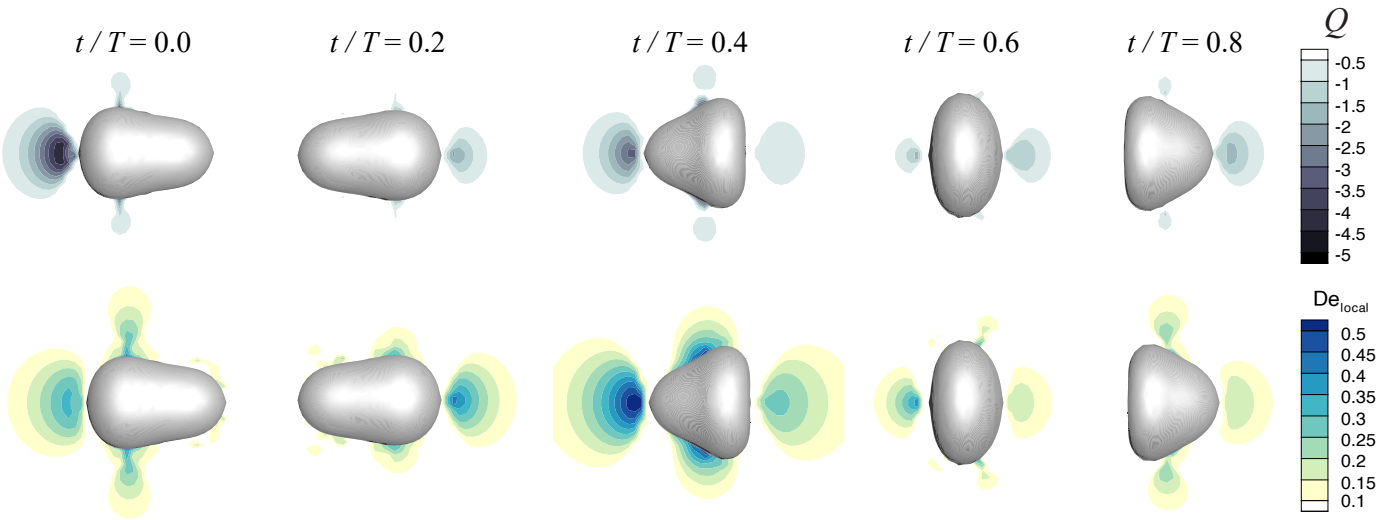

Fig. 18 Extensional flow strength for the amoeba simulations at $\beta = 0.75$, $\mathrm{De} = 0.25$. We use an eigenvalue analysis[58,59] to obtain a qualitative picture of extensional flow around the amoeba. To denote the strength of the local extensional flow, we plot the value of $Q = \frac{1}{2}[(\mathrm{tr}(\bar{\nabla}\bar{\mathbf{v}})^2 - \mathrm{tr}(\bar{\nabla}\bar{\mathbf{v}}^2)]$ in the flow field when $D < 0$ since $D = (27/4)R^2 + Q^3 < 0$ denotes regions of extension. As described in the text, the tensor invariant Q measures the relative strength of rotation and strain of the local flow. We see that the regions of greatest extension are located at many points near the body depending on what part of the cycle the amoeboid is currently in, which explains why we see extension in a boundary layer around almost the entire surface in Fig. 16. In the second row the local De number is plotted for the same time snapshots. The local Deborah number is the maximum extensional eigenvalue times the relaxation time of the fluid. We see De numbers in excess of 0.5 which means the we have passed the coil-stretch transition indicating these flows are sufficiently strong to be generating stretch even for the low $\mathrm{De} = 0.25$. All snapshots presented are at the $(z = 0)$ center plane and at steady state.

cal De number to be the maximum rate of extension (the largest positive eigenvalue of the local velocity gradient) at each point multiplied by the fluid relaxation time. We see that even at the modest $\mathrm{De} = 0.25$ that the local De number exceeds 0.5 so the polymer will extend substantially due to the flow exceeding the required local De number for the coil-stretch transition.

It is also very unlikely that these polymer stretch regions result from shear or the translational motion of the swimmer. If we consider the amoeboid simulation with most polymer stretch, $\mathrm{De} = 5$ and $\beta = 0.25$, we find that the resulting stretch from the shear generated by translational motion will be very small. For this swimmer, $U/(R_p f) \approx 0.024$ since $U/U_N \approx 0.2$ from Fig. 15 and $U_N/(R_p f) = 0.12$ (the dimensionless speed in a Newtonian fluid). Thus an associated Wi based on this swimming speed would be $\mathrm{Wi} = \lambda U/R_p = 0.12$. If we consider the equivalent steady shear flow with an Oldroyd-B fluid c_{ii} is $3 + 2\mathrm{Wi}^2 \approx 0.03$[48]. Recall for the Oldroyd-B model that the polymer stress energy is $\bar{\sigma}^p_{ii} = \frac{1-\beta}{\mathrm{Wi}}(c_{ii} - 3) \approx 0.18$ which is an order of magnitude smaller than the greatest stretch in Fig. 16, illustrating that these regions of high stretch are not a result of local shear but almost certainly due to the local extensions seen in Fig. 18.

Lastly, we also examine other features of the amoeba's swimming motion in a viscoelastic fluid such as the effect fluid elasticity has on its power expenditure and its average swimming efficiency. We see that not only does the amoeba swim more slowly, but it also exhibits a marked decrease in swimming efficiency since it still expends roughly the same amount of power to swim. In Fig. 19 we plot both the efficiency and the power vs. De for three different values of β. We can see that power, which is expressed as $P = \frac{1}{T}\int_0^T \int \boldsymbol{f}^{\mathrm{act}} \cdot \mathbf{u} \mathrm{d}S\mathrm{d}t$, shows a very modest reduction as the De is increased. Because the swimmer spends almost the same amount of energy to move despite it swimming significantly more slowly as the De increases, the overall efficiency $\eta_{\mathrm{e}} = P/(6\pi\eta a U^2)$ is reduced considerably with increasing fluid elasticity.

4 Conclusions

In this study, we have explored the effect of fluid elasticity on two "model" swimming motions: the undulatory motion of *C. elegans* and amoeboid motion. Notably, we have performed the first fully three-dimensional simulations of these types of swimmers in viscoelastic fluids , including a complete study of the effect of the elastic fluid viscosity ratio, β, yielding new insights that could not be captured in previous theoretical or numerical analyses.

For both swimmers, despite the clear differences in the way that they propel themselves, we find a monotonic reduction in swimming speed to an asymptotic plateau value as the Deborah number (De) increases. For the motion of *C. elegans* in particular, we find regions of large polymer stress concentrated at the head and tail of the swimmer. Using local invariants of the flow field, we showed that these regions for the finite De simulations are likely created by strong extensional flow at these locations throughout the swim cycle. Interestingly, we found that this is qualitatively different from predictions of recent 2D simulations, where the polymer stress is high around the entire immersed body. We suggest this is a potential reason why the swimming speeds in a viscoelastic fluid normalized by that in a Newtonian fluid are larger in the 3D simulations than those produced from previous 2D numerical studies. We also find from our speed reduction curves that the normalized speed at large De appears to scale linearly with β. An examination of the polymer stress energy in the flow field as a function of β shows little change in the distribution of

View Article Online
DOI: 10.1039/C8SM02518E

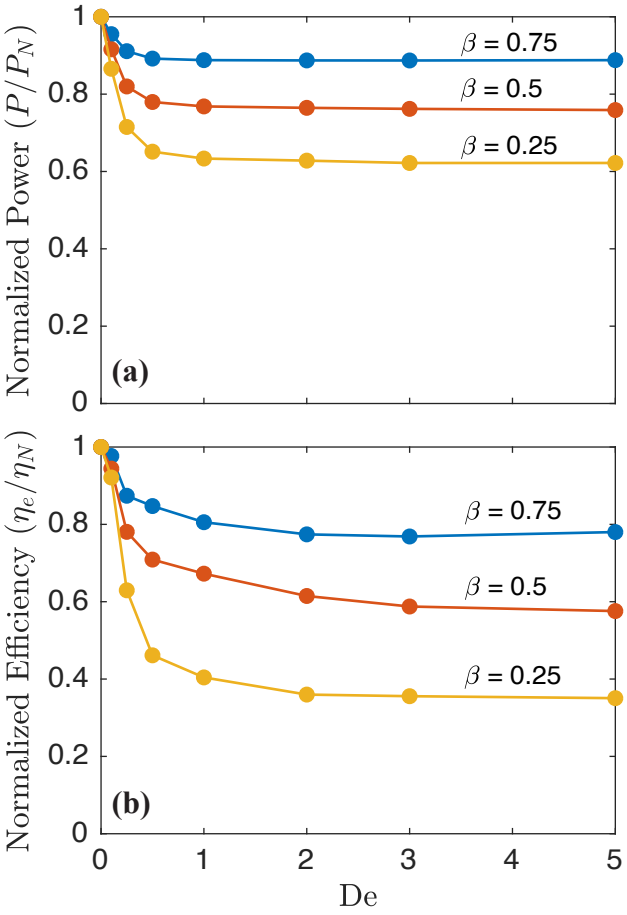

Fig. 19 Average power (P) and efficiency (η_e) normalized by their values in a Newtonian fluid for the amoeboid simulations. We see that not only does the amoeba swimmer move more slowly with increasing De and β (Fig. 15), but it also expends less power (the hydrodynamic power for the amoeboid is defined as $P = \int_S \boldsymbol{f}^{\text{act}} \cdot \mathbf{u} dS$). Because the reduction in power expenditure is smaller than the reduction in speed for all De and β, the net effect is that the swimming efficiency in a viscoelastic fluid is always less than that for a Newtonian fluid (the swimming efficiency is defined as the ratio of the hydrodynamic power of the amoeba to the power needed to translate a sphere with the same volume and average speed: $\eta_e = P/(6\pi\eta a U^2)$).

this stress as β is varied. Thus, we believe that the effect to which fluid elasticity has on the swimming speed does not change with β; rather, β only modulates the degree to which it influences the swimming speed.

For the case of amoeboid motion, we show that a decrease in swimming speed is correlated with an accumulation of polymer stress that surrounds the deforming body. We hypothesize that since the amoeboid is confined to swim in a straight line unlike *C. elegans*, that it is unable to avoid the polymeric stress that it incurs as the generated flow deforms polymers in the fluid. In contrast, the *C. elegans* swimmer is constantly undulating laterally relative to its net direction of motion; we think this is the reason the normalized speeds for the amoeba are smaller than those for *C. elegans* simulations. We find that the asymptotic swimming speed at large values of De appears to be a nearly linear function of β as we found for *C. elegans*. This suggests that for both organisms the effect of fluid elasticity scales in direct proportion to the concentration of polymer in solution.

In conclusion, we have demonstrated that the dynamics of deformable swimmers in complex fluids can be accurately studied using a modified 3D Immersed Finite Element Method. The flow solver and immersed boundary code has been extensively validated in previous studies[49] and has been applied to kinematically controlled and force controlled swimming motions. The force controlled studies have been benchmarked against previous Newtonian flow studies, further suggesting the accuracy of this proposed method[46]. Since this simulation tool is capable of simulating multiple deformable swimmers in arbitrarily complex geometries, we believe that this algorithm can aid other researchers in future studies of swimming in viscoelastic fluids.

Acknowledgements

The authors of this paper would like to acknowledge support from NSF (CBET-1803765) and support from the US Army High Performance Computation Research Center (AHPCRC) with the grant number W911NF07200271. Computer simulations were also performed on the Stanford University Certainty computer cluster, which is funded by the American Recovery and Reinvestment Act of 2009.

The authors would also like to thank Paulo Arratia for his experimental data and helpful conversations concerning experiments with *C. elegans*.

Conflicts of Interest

There are no conflicts of interest to declare.

References

1 S. S. Suarez and A. A. Pacey, *Human Reproduction Update*, 2006, **12**, 23–37.
2 J. W. Costerton, P. S. Stewart and E. P. Greenberg, *Science*, 1999, **284**, 1318–1322.
3 S. K. Lai, Y.-Y. Wang, D. Wirtz and J. Hanes, *Advanced Drug Delivery Reviews*, 2009, **61**, 86–100.
4 R. Dreyfus, J. Baudry, M. L. Roper, M. Fermigier, H. A. Stone and J. Bibette, *Nature*, 2005, **437**, 862–865.
5 J. R. Howse, R. A. L. Jones, A. J. Ryan, T. Gough, R. Vafabakhsh and R. Golestanian, *Physical Review Letters*, 2007, **99**, 8–11.
6 L. Zhang, J. J. Abbott, L. Dong, B. E. Kratochvil, D. Bell and B. J. Nelson, *Applied Physics Letters*, 2009, **94**, 2007–2010.
7 A. Ghosh and P. Fischer, *Nano Letters*, 2009, **9**, 2243–2245.
8 S. J. Ebbens and J. R. Howse, *Soft Matter*, 2010, **6**, 726–738.
9 D. Patra, S. Sengupta, W. Duan, H. Zhang, R. Pavlick and A. Sen, *Nanoscale*, 2013, **5**, 1273–1283.
10 K. E. Peyer, L. Zhang and B. J. Nelson, *Nanoscale*, 2013, **5**, 1259–72.
11 B. J. Williams, S. V. Anand, J. Rajagopalan and M. T. A. Saif, *Nature Communications*, 2014, **5**, 3081.
12 S. Sanchez, L. Soler and J. Katuri, *Angewandte Chemie - International Edition*, 2015, **54**, 1414–1444.

View Article Online
DOI: 10.1039/C8SM02518E

13 G. Li and A. M. Ardekani, *Journal of Fluid Mechanics*, 2015, **784**, R4.
14 C. Li, B. Qin, A. Gopinath, P. E. Arratia, B. Thomases and R. D. Guy, *Journal of the Royal Society Interface*, 2017, **14**, 20170289.
15 A. Joseph, C. Contini, D. Cecchin, S. Nyberg, L. Ruiz-Perez, J. Gaitzsch, G. Fullstone, X. Tian, J. Azizi, J. Preston, G. Volpe and G. Battaglia, *Science Advances*, 2017, **3**, e1700362.
16 E. M. Purcell, *American Journal of Physics*, 1977, **45**, 3–11.
17 E. Lauga and T. R. Powers, *Rep. Prog. Phys.*, 2009, **72**, 96601–36.
18 J. Elgeti, R. G. Winkler and G. Gompper, *Reports on Progress in Physics*, 2015, **78**, 056601.
19 C.-k. Tung, C. Lin, B. Harvey, A. G. Fiore, F. Ardon, M. Wu and S. S. Suarez, *Scientific Reports*, 2017, **7**, 3152.
20 J. Sznitman and P. E. Arratia, in *Locomotion Through Complex Fluids: An Experimental View*, ed. S. E. Spagnolie, Springer New York, New York, NY, 2015, pp. 245–281.
21 J. Sznitman, X. Shen, R. Sznitman and P. E. Arratia, *Physics of Fluids*, 2010, **22**, 121901.
22 T. D. Montenegro-Johnson, D. A. Gagnon, P. E. Arratia and E. Lauga, *Physical Review Fluids*, 2016, **1**, 053202.
23 X. N. Shen and P. E. Arratia, *Physical Review Letters*, 2011, **106**, 208101.
24 D. A. Gagnon, N. C. Keim and P. E. Arratia, *J. Fluid Mech.*, 2014, **758**, R3.
25 D. A. Gagnon and P. E. Arratia, *Journal of Fluid Mechanics*, 2016, **800**, 753–765.
26 G. I. Taylor, *Proceedings of the Royal Society of London A: Mathematical, Physical and Engineering Sciences*, 1951, **209**, 447–461.
27 E. Lauga, *Physics of Fluids*, 2007, **19**, 083104.
28 E. E. Riley and E. Lauga, *Journal of Theoretical Biology*, 2015, **382**, 345–355.
29 E. E. Riley and E. Lauga, *EPL (Europhysics Letters)*, 2014, **108**, 34003.
30 H. C. Fu, T. R. Powers and C. W. Wolgemuth, *Physical Review Letters*, 2007, **99**, 258101.
31 H. C. Fu, C. W. Wolgemuth and T. R. Powers, *Physical Review E - Statistical, Nonlinear, and Soft Matter Physics*, 2008, **78**, 041913.
32 J. Teran, L. Fauci and M. Shelley, *Physical Review Letters*, 2010, **104**, 038101.
33 B. Thomases and R. D. Guy, *Physical Review Letters*, 2014, **113**, 098102.
34 R. D. Guy and B. Thomases, *Complex Fluids in Biological Systems*, Springer New York, 2015, pp. 359–397.
35 D. Salazar, A. M. Roma and H. D. Ceniceros, *Physics of Fluids*, 2016, **28**, 063101.
36 T. D. Montenegro-Johnson, *Physical Review Fluids*, 2017, **2**, 053202.
37 C. Li, B. Thomases and R. D. Guy, *Phys. Rev. Fluids*, 2019, **4**, 031301.
38 H. C. Fu, C. W. Wolgemuth and T. R. Powers, *Physics of Fluids*, 2009, **21**, 033102.
39 B. Liu, T. R. Powers and K. S. Breuer, *Proceedings of the National Academy of Sciences*, 2011, **108**, 19516–19520.
40 S. E. Spagnolie, B. Liu and T. R. Powers, *Physical Review Letters*, 2013, **111**, 068101.
41 N. P. Barry and M. S. Bretscher, *Proceedings of the National Academy of Sciences*, 2010, **107**, 11376–11380.
42 P. J. van Haastert, *PLoS ONE*, 2011, **6**, e27532.
43 A. Farutin, S. Rafaï, D. K. Dysthe, A. Duperray, P. Peyla and C. Misbah, *Physical Review Letters*, 2013, **111**, 1–5.
44 H. Wu, M. Thiébaud, W. F. Hu, A. Farutin, S. Rafaï, M. C. Lai, P. Peyla and C. Misbah, *Physical Review E - Statistical, Nonlinear, and Soft Matter Physics*, 2015, **92**, 050701.
45 H. Wu, A. Farutin, W.-F. F. Hu, M. Thiébaud, S. Rafaï, P. Peyla, M.-C. C. Lai and C. Misbah, *Soft Matter*, 2016, **12**, 7470–7484.
46 M. Ranganathan, A. Farutin and C. Misbah, *Biophysical Journal*, 2018, 1316–1329.
47 B. Thomases and R. D. Guy, *Journal of Fluid Mechanics*, 2017, **825**, 109–132.
48 R. B. Bird, R. C. Armstrong and O. Hassager, *Dynamics of Polymeric Liquids. Vol. 1: Fluid mechanics*, Wiley, 1987.
49 A. Saadat, C. J. Guido, G. Iaccarino and E. S. G. Shaqfeh, *Physical Review E*, 2018, **98**, 063316.
50 F. Ham, K. Mattsson and G. Iaccarino, *Annual Research Briefs*, 2006, 243–261.
51 R. Fattal and R. Kupferman, *Journal of Non-Newtonian Fluid Mechanics*, 2004, **123**, 281–285.
52 M. A. Hulsen, R. Fattal and R. Kupferman, *Journal of Non-Newtonian Fluid Mechanics*, 2005, **127**, 27–39.
53 M. Yang, S. Krishnan and E. S. G. Shaqfeh, *J. of Non-Newton. Fluid Mech.*, 2016, **234**, 51–68.
54 D. Richter, G. Iaccarino and E. S. G. Shaqfeh, *J. Fluid Mech.*, 2010, **651**, 415–442.
55 S. Padhy, E. S. G. Shaqfeh, G. Iaccarino, J. F. Morris and N. Tonmukayakul, *J. Non-Newton. Fluid Mech.*, 2013, **197**, 48–60.
56 P. Bagchi and R. M. Kalluri, *Phys. Rev. E*, 2009, **80**, 16307.
57 S. Mendez, E. Gibaud and F. Nicoud, *J. Comput. Phys.*, 2014, **256**, 465–483.
58 V. E. Terrapon, Y. Dubief, P. Moin, E. S. G. Shaqfeh and S. K. Lele, *Journal of Fluid Mechanics*, 2004, **504**, 61–71.
59 A. Ooi, J. Martin, J. Soria and M. S. Chong, *Journal of Fluid Mechanics*, 1999, **381**, 141–174.
60 E. Lauga, *Physical Review E - Statistical, Nonlinear, and Soft Matter Physics*, 2007, **75**, 041916.
61 M. S. Chong, A. E. Perry and B. J. Cantwell, *Physics of Fluids A: Fluid Dynamics*, 1990, **2**, 765–777.
62 J. R. Vélez-Cordero and E. Lauga, *Journal of Non-Newtonian Fluid Mechanics*, 2013, **199**, 37–50.
63 E. Lauga, *Physics of Fluids*, 2014, **26**, 101307.
64 H. Giesekus, *Journal of Non-Newtonian Fluid Mechanics*, 1982, **11**, 69 – 109.

View Article Online
DOI: 10.1039/C8SM02518E

We explore swimming speeds of *C. elegans* and amoeboids in viscoelastic fluids with three-dimensional, large amplitude simulations.